

Indoor Transmission of Respiratory Droplets Under Different Ventilation Systems Using the Eulerian Approach for the Dispersed Phase

*Original*

Indoor Transmission of Respiratory Droplets Under Different Ventilation Systems Using the Eulerian Approach for the Dispersed Phase / Feng, Yi; Li, Dongyue; Marchisio, Daniele; Vanni, Marco; Buffo, Antonio. - In: FLUIDS. - ISSN 2311-5521. - 10:7(2025). [10.3390/fluids10070185]

*Availability:*

This version is available at: 11583/3005672 since: 2025-12-05T15:22:15Z

*Publisher:*

Multidisciplinary Digital Publishing Institute (MDPI)

*Published*

DOI:10.3390/fluids10070185

*Terms of use:*



This article is made available under terms and conditions as specified in the corresponding bibliographic description in the repository

*Publisher copyright*

(Article begins on next page)

## Article

# Indoor Transmission of Respiratory Droplets Under Different Ventilation Systems Using the Eulerian Approach for the Dispersed Phase

Yi Feng <sup>1</sup> , Dongyue Li <sup>2</sup> , Daniele Marchisio <sup>1</sup> , Marco Vanni <sup>1</sup>  and Antonio Buffo <sup>1,\*</sup> 

<sup>1</sup> Department of Applied Science and Technology, Politecnico di Torino, Corso Duca degli Abruzzi 24, 10129 Torino, Italy; yi.feng@polito.it (Y.F.); danielle.marchisio@polito.it (D.M.); marco.vanni@polito.it (M.V.)

<sup>2</sup> DYFLUID Ltd., Beijing 100029, China; li.dy@dyfluid.com

\* Correspondence: antonio.buffo@polito.it

## Abstract

Infectious diseases can spread through virus-laden respiratory droplets exhaled into the air. Ventilation systems are crucial in indoor settings as they can dilute or eliminate these droplets, underscoring the importance of understanding their efficacy in the management of indoor infections. Within the field of fluid dynamics methods, the dispersed droplets may be approached through either a Lagrangian framework or an Eulerian framework. In this study, various Eulerian methodologies are systematically compared against the Eulerian–Lagrangian (E-L) approach across three different scenarios: the pseudo-single-phase model (PSPM) for assessing the transport of gaseous pollutants in an office with displacement ventilation (DV), stratum ventilation (SV), and mixing ventilation (MV); the two-fluid model (TFM) for evaluating the transport of non-evaporating particles within an office with DV and MV; and the two-fluid model–population balance equation (TFM-PBE) approach for analyzing the transport of evaporating droplets in a ward with MV. The Eulerian and Lagrangian approaches present similar agreement with the experimental data, indicating that the two approaches are comparable in accuracy. The computational cost of the E-L approach is closely related to the number of tracked droplets; therefore, the Eulerian approach is recommended when the number of droplets required by the simulation is large. Finally, the performances of DV, SV, and MV are presented and discussed. DV creates a stratified environment due to buoyant flows, which transport respiratory droplets upward. MV provides a well-mixed environment, resulting in a uniform dispersion of droplets. SV supplies fresh air directly to the breathing zone, thereby effectively reducing infection risk. Consequently, DV and SV are preferred to reduce indoor infection.

**Keywords:** Eulerian approach; Eulerian–Lagrangian approach; population balance equation; respiratory droplets; ventilation systems



Academic Editors: Pengtao Yue and Xinguang Cui

Received: 30 May 2025

Revised: 3 July 2025

Accepted: 10 July 2025

Published: 14 July 2025

**Citation:** Feng, Y.; Li, D.; Marchisio, D.; Vanni, M.; Buffo, A. Indoor Transmission of Respiratory Droplets Under Different Ventilation Systems Using the Eulerian Approach for the Dispersed Phase. *Fluids* **2025**, *10*, 185. <https://doi.org/10.3390/fluids10070185>

**Copyright:** © 2025 by the authors. Licensee MDPI, Basel, Switzerland. This article is an open access article distributed under the terms and conditions of the Creative Commons Attribution (CC BY) license (<https://creativecommons.org/licenses/by/4.0/>).

## 1. Introduction

Some infectious diseases can be transmitted by virus-laden respiratory droplets exhaled by an infected person [1]. Since people spend most of their time in indoor environments [2], such as offices, classrooms, and hospital wards, studies on the transmission of respiratory droplets in these scenarios are important to control infections.

Respiratory droplets in indoor environments form a complex multiphase system influenced by factors such as droplet composition, size, and ambient conditions. Droplets, ranging from micrometers to millimeters in size, exhibit varying dynamics under forces

such as drag and gravity [3]. They partially evaporate due to their volatile and non-volatile components; smaller droplets often transform into nuclei [4], while larger ones settle quickly under gravity [5]. Beyond droplet dynamics, indoor layouts, including furniture and barriers, significantly influence deposition and trajectories [6]. Ambient conditions, such as temperature and relative humidity (RH), alter airflow properties and evaporation rates, thus affecting disease transmission dynamics [7]. By shaping indoor airflow patterns, ventilation systems mitigate infection risks by diluting or removing virus-laden droplets.

In recent years, the performance of various ventilation systems in diluting and removing virus-laden respiratory droplets has been extensively studied. Experimental investigations have predominantly employed two methods: the tracer gas method and the tracer particle (or droplet) method [8]. The tracer gas method involves measuring the concentration of selected gases, such as CO<sub>2</sub> [9], N<sub>2</sub>O [10,11], or SF<sub>6</sub> [12,13], to evaluate the transmission of gaseous pollutants. Small respiratory droplets or aerosols, which tend to follow background airflow because of their size, exhibit behavior comparable to that of tracer gases. Thus, tracer gases are also suitable for tracking aerosol transmission, especially aerosols with sizes around 1 μm [14–16]. For example, Tian et al. [17] used CO<sub>2</sub> to assess the performance of mixing ventilation (MV), displacement ventilation (DV), and stratum ventilation (SV) in a small office, finding that SV removed CO<sub>2</sub> more effectively in the breathing zone compared to MV and DV. Ameen et al. [18] compared tracer gas (SF<sub>6</sub>) decay in corner-impinging jet ventilation with MV and DV, revealing the superior air exchange effectiveness of this method. Moreover, Kong et al. [19,20] employed CO<sub>2</sub> in experimental studies of novel ventilation systems, including low-temperature radiant floors coupled with intermittent stratum ventilation and interactive cascade ventilation. These innovative systems demonstrated enhanced performance in reducing infection risks.

The tracer particle method measures the concentration of particles to approximate the behavior of respiratory droplets. Compared to the tracer gas method, it offers a closer representation of respiratory droplets by employing polydispersed evaporating particles or droplets. For example, Zhou et al. [21] investigated aerosol transmission in a ventilated fever clinic using particles ranging from 0.1 μm to 10 μm. Their study revealed that the location of the occupants significantly influenced the effectiveness of aerosol removal. Similarly, Liu et al. [22] studied the performance of mixing ventilation and displacement ventilation using particles in the range of 0.3 μm to 2 μm. Their findings demonstrated that DV produced a vertical stratification of particle concentration, leading to better air quality than MV. Zhuang et al. [23] used solid particles (<10 μm) to examine the underfloor air distribution. They observed distinct behaviors: fine particles (<2.5 μm) exhibited suspension trends, while coarse particles (>2.5 μm) showed settling tendencies. In addition, tracer droplets have been used to mimic respiratory droplet evaporation. Xu et al. [24] employed evaporating salt-water droplets (0.3 μm to 10 μm) to evaluate three customized ventilation systems. Wang et al. [25] studied evaporating droplets (0.3 μm to 5 μm) in a negative-pressure isolation ward under MV. Their results indicated that smaller droplets quickly evaporated into nuclei, resulting in similar size distributions across different locations in the ward.

The above experimental studies reveal the performance of different ventilation systems in removing respiratory aerosols or droplets. However, due to the limited number of measuring points, experimental studies may not fully capture the non-uniform distribution of respiratory droplets caused by complex indoor airflow patterns under various ventilation systems [26]. To address this limitation, numerical methods are increasingly utilized to provide detailed temporal evolution and spatial distribution of respiratory droplets. These methods enable a comprehensive analysis of droplet dynamics and their interactions with

airflow, furnishing valuable insights for optimizing indoor ventilation strategies to control infection risks.

As shown in Figure 1, respiratory droplets vary significantly in size, ranging from micrometers to millimeters. These droplets can be either polydispersed, exhibiting a wide size range with diverse behaviors, or monodispersed, distributed within a narrow size range and demonstrating similar dynamics. Depending on their size and distribution, different numerical methods can be employed for their simulation: the Lagrangian approach or Eulerian approaches of various complexities. The Lagrangian approach tracks dispersed droplets individually by solving specific evolution equations for their motion and size changes while treating the air phase as a continuum through the Navier–Stokes (N-S) equations. This combined method, often referred to as the Eulerian–Lagrangian (E-L) approach, excels in modeling both monodispersed and polydispersed evaporating droplets with wide size distributions. Consequently, the E-L approach has been extensively used for simulating droplet transport and evaporation under various ventilation systems [27–32].

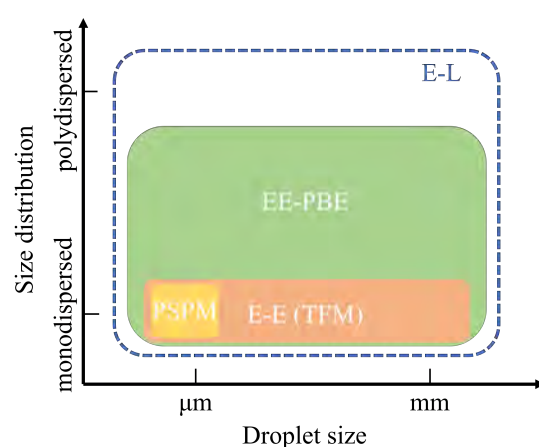


**Figure 1.** Different numerical methods for the transmission of respiratory droplets.

For instance, Wang et al. [33] utilized the E-L approach to simulate droplet behavior (1  $\mu\text{m}$  to 100  $\mu\text{m}$ ) under impinging jet ventilation and two forms of mixing ventilation. Similarly, Ren et al. [34] applied this approach to trace droplets with diameters ranging from 3 to 175  $\mu\text{m}$  in ventilated wards, while Liu and Deng [35] simulated the transmission of dry droplet nuclei (0.75  $\mu\text{m}$  to 330  $\mu\text{m}$ ) in an elevator equipped with MV. In these studies, the E-L approach accurately predicted the fate of droplets of various sizes, with larger droplets depositing on surfaces and smaller ones being effectively removed by the ventilation systems.

Also, the evaporation of respiratory droplets can be effectively modeled using the E-L approach. For example, Borro et al. [36] traced the dispersion of evaporating droplets ranging from 3  $\mu\text{m}$  to 750  $\mu\text{m}$  in a ventilated hospital room. Similarly, Li and Feng [37] investigated the transmission of evaporating droplets (1  $\mu\text{m}$  to 1500  $\mu\text{m}$ ) under air curtain, MV, and DV configurations. Lu and Lin [38] incorporated evaporation into their simulation of cough droplet dispersion in a ward equipped with DV, SV, and MV. In particular, Zhang et al. [39] utilized large eddy simulation for the continuous phase and the Lagrangian approach for the dispersed phase to study droplet transport and evaporation during coughing and talking in a room with MV and DV. Their model simulated droplets with initial sizes of 1, 10, 20, 50, and 100  $\mu\text{m}$ , demonstrating distinct dynamics: 100  $\mu\text{m}$  droplets initially moved downward due to gravity, but as they evaporated to smaller sizes, buoyant airflow in DV caused upward movement. These studies underscore the significant effects of evaporation and polydispersity on droplet trajectories, highlighting the necessity of considering both factors in respiratory droplet transmission models.

To achieve stochastically stable results, the E-L approach requires tracking a sufficiently large number of particles to ensure statistical convergence of the simulated droplet dynamics. This need arises because the approach relies on the random sampling of particle trajectories, and an insufficient number of particles can introduce significant variability in the results. Clearly, the computational cost increases with the number of tracked particles and may become substantial when highly accurate simulations are required. Consequently, the Eulerian–Eulerian (E-E) approach has gained attention for its lower computational demands [40]. This approach models dispersed respiratory droplets as a continuum, employing various strategies to compute droplet velocities. The simplest method, the pseudo-single-phase model (PSPM), assumes that droplets, regardless of size, follow the airflow exactly. In this case, only the Navier–Stokes equations for the continuous phase are solved, with an additional scalar transport equation representing droplet concentration [41] or species mass fraction [42]. Similar to the tracer gas method, the PSPM is limited to modeling small droplets or aerosols, as shown in Figure 1. Due to its simplicity, this model is widely applied in studies of ventilation systems [43–46].

For larger droplets that do not entirely follow the airflow, the solution requires an additional momentum balance equation for the dispersed phase. The two-fluid model (TFM), a widely used E-E approach, treats droplets as a continuum and solves momentum equations for both gas and droplet phases, incorporating interphase momentum transport due to interfacial forces. Yan et al. [47] compared the TFM with the E-L approach in studying particle transport under displacement ventilation (DV), finding comparable accuracy in predicting flow fields, though the E-L approach better modeled particle–wall interactions. Similarly, Pei et al. [48] contrasted the TFM and PSPM in simulating aerosol transmission (1  $\mu\text{m}$  and 10  $\mu\text{m}$ ) under DV and MV. Their results showed that the TFM provided more detailed concentration distributions for larger aerosols, revealing lower concentrations due to deposition. Moreover, simplified E-E models, such as the mixture model [49] and the drift-flux model [49–51], were also used to simulate respiratory droplet transport.

Despite its relatively lower computational costs, the Eulerian–Eulerian (E-E) approach has not been as widely adopted as the Eulerian–Lagrangian (E-L) method. As shown in Figure 1, the E-E approach is generally applied to monodispersed droplets, though it is also capable of describing polydisperse evaporating droplets. To address this limitation, we previously coupled the population balance equation (PBE) with the E-E approach, enabling the simulation of both droplet size evolution and transport [52]. This EE-PBE (TFM-PBE) approach was validated against experimental and numerical data, demonstrating its capability to model the transport of evaporating droplets in a room without ventilation systems.

Given the computational efficiency of Eulerian approaches, they remain promising tools for studying respiratory droplet dynamics in indoor ventilation systems. This study extends the application of Eulerian methods, including the TFM-PBE approach, to simulate evaporating respiratory droplets, an area traditionally modeled using E-L methods. Additionally, a systematic benchmark comparison is conducted between Eulerian and E-L approaches across a range of realistic ventilated indoor environments. These environments are modeled using tailored Eulerian approaches: the pseudo-single-phase model (PSPM) for gaseous pollutants, the two-fluid model (TFM) for non-evaporating monodispersed particles, and the TFM-PBE approach for evaporating polydispersed droplets. By focusing on computational efficiency and accuracy, this work demonstrates the capability of Eulerian methods to provide robust alternatives to E-L approaches, offering valuable insights into the optimization of ventilation systems for infection control.

The manuscript is arranged as follows: Section 2 introduces the Eulerian and Lagrangian approaches, including the pseudo-single-phase model (PSPM), the two-fluid

model (TFM), the TFM-PBE coupled approach, and the Eulerian–Lagrangian approach. Section 3 details the application of these Eulerian approaches to respiratory droplet transport in ventilated indoor environments, with comparisons to the Lagrangian approach. Finally, Section 4 provides the conclusions derived from this study.

## 2. Methodology

### 2.1. Pseudo-Single-Phase Model

In the PSPM, small respiratory particles are regarded as passive tracers following the airflow due to their small sizes. Therefore, their velocity can be obtained by solving the N-S equations of the airflow. The evolution of the particles is tracked by solving a scalar transport equation representing the mass fraction of the particles, which can be written as [42]:

$$\frac{\partial}{\partial t}(\rho Y_p) + \nabla \cdot (\rho \mathbf{U} Y_p) - \nabla \cdot (D_{\text{Eff},p} \nabla Y_p) = 0, \tag{1}$$

where  $Y_p$  is the mass fraction of particles in the air phase;  $\rho$  is the air density;  $\mathbf{U}$  is the velocity of the airflow;  $D_{\text{Eff},p}$  is the effective diffusion coefficient equal to the sum of the Brownian contribution ( $D_p$ ) and the turbulent contribution ( $\mu_t/Sc_t$ ), and the default value for the turbulent Schmidt number  $Sc_t$  is 0.7. While the PSPM is suitable for modeling small respiratory aerosols that closely follow airflow, larger droplets with significant inertia require the two-fluid model to account for interphase interactions.

### 2.2. Two-Fluid Model

The two-fluid model (TFM) treats both the continuous and dispersed phases as interpenetrating continua, solving separate sets of governing equations for each phase. The dispersed phase is described using equations for continuity, momentum, and energy [53]:

$$\frac{\partial}{\partial t}(\alpha_d \rho_d) + \nabla \cdot (\alpha_d \rho_d \mathbf{U}_d) = \dot{m}_d, \tag{2}$$

$$\frac{\partial}{\partial t}(\alpha_d \rho_d \mathbf{U}_d) + \nabla \cdot (\alpha_d \rho_d \mathbf{U}_d \otimes \mathbf{U}_d) = -\alpha_d \nabla p + \nabla \cdot (\alpha_d \mathbf{R}_{\text{Eff},d}) + \alpha_d \rho_d \mathbf{g} + \mathbf{F}_d + \dot{\mathbf{M}}_d, \tag{3}$$

$$\frac{\partial}{\partial t}(\alpha_d \rho_d (E_d + K_d)) + \nabla \cdot (\alpha_d \rho_d \mathbf{U}_d (E_d + K_d)) = \nabla \cdot (\alpha_d a_{\text{Eff},d} \nabla E_d) - \alpha_d \nabla \cdot (p \mathbf{U}_d) + \alpha_d \rho_d \mathbf{g} \cdot \mathbf{U}_d + \dot{Q}_d, \tag{4}$$

where the subscripts c and d represent the continuous phase and the dispersed phase, respectively. Therefore,  $\alpha_d$ ,  $\rho_d$  and  $\mathbf{U}_d$  are the dispersed phase volume fraction, density and velocity. The term  $\dot{m}_d$  is the mass transfer rate per unit volume due to evaporation or condensation. The pressure  $p$  is shared by the continuous and dispersed phase. The term  $\mathbf{R}_{\text{Eff},d}$  is the effective stress tensor containing laminar and turbulent contribution;  $\mathbf{g}$  is the gravitational acceleration vector;  $\mathbf{F}_d$  is the interphase force term;  $\dot{\mathbf{M}}_d$  is the momentum transfer rate caused by mass transfer;  $E_d$  is the sensible internal energy and  $K_d$  is the kinetic energy;  $a_{\text{Eff},d}$  is the effective thermal diffusivity; and  $\dot{Q}_d$  contains the interphase heat transfer and the energy transfer caused by mass transfer. These equations describe the transport and interactions of droplets within the air phase, accounting for interphase momentum, mass, and heat transfer. More details on the interphase models for the TFM can be found in our previous work [52].

The droplet velocity,  $\mathbf{U}_d$ , depends on the droplet size and can be identical to the air velocity  $\mathbf{U}_c$  or different from it. Therefore, TFM can be used to track the transport of larger droplets that do not passively follow the airflow. The TFM assumes a single droplet size at any given location, typically using the mean diameter for interphase calculations. Although this simplifies the model, it limits its ability to describe polydispersed systems.

In such cases, coupling the TFM with the population balance equation (PBE) enables the representation of droplet size distributions, as described in the next subsection.

### 2.3. Population Balance Equation

The population balance equation (PBE) describes the evolution of the droplet size distribution (DSD),  $n(t, \mathbf{x}, d)$ , where  $n$  represents the number density of droplets at time  $t$ , spatial position  $\mathbf{x}$ , and droplet diameter  $d$  [54]. The general form of the PBE is

$$\frac{\partial n(d)}{\partial t} + \nabla \cdot [\mathbf{U}(d)n(d)] + \frac{\partial}{\partial d}[G(d)n(d)] = 0, \tag{5}$$

where the variable  $G = dd/dt$  is the rate of change of droplet size due to condensation or evaporation and  $\mathbf{U}$  is the droplet velocity. In this work, coalescence and breakup processes are neglected, as they play a minor role in the transport of dilute aerosols by ventilation systems. Equation (5) is consistent with the monokinetic assumption, which means that droplets of the same size  $d$  share the same velocity  $\mathbf{U}(d)$  at a given location  $\mathbf{x}$ , neglecting cross-particle trajectories. In order to take into account the full statistical distribution of velocity, a much more complex approach must be used, which is discussed in our previous work [52] but is not adopted here.

The PBE is solved using the Quadrature Method of Moments (QMOM), which approximates the DSD  $n(t, \mathbf{x}, d)$  as a weighted sum of Dirac delta functions:

$$n(t, \mathbf{x}, d) \approx \sum_{p=1}^N w_p(t, \mathbf{x})\delta(d - d_p(t, \mathbf{x})), \tag{6}$$

where  $w_p(t, \mathbf{x})$  and  $d_p(t, \mathbf{x})$  are the weight and abscissa of the  $p$ th node and  $N$  is the number of quadrature nodes. The  $k$ -th order moment of the DSD,  $M_k$ , can be expressed as

$$M_k = \int_0^{+\infty} d^k n(d) dd \approx \sum_{p=1}^N w_p d_p^k. \tag{7}$$

Equation (7) implies that the  $N$  unknown weights  $w_p$  and the  $N$  unknown abscissas  $d_p$  can be calculated using the first  $2N$  moments, and the moments are obtained by solving the moment transport equations. Multiplying Equation (5) with  $d^k$  and integrating it with respect to the diameter  $d$  yields the transport equation for the  $k$ -th order moment  $M_k$ :

$$\frac{\partial M_k}{\partial t} + \nabla \cdot \int_0^{+\infty} d^k n(d)\mathbf{U}(d) dd + \int_0^{+\infty} d^k \frac{\partial}{\partial d}(G(d)n(d)) dd = 0, \tag{8}$$

where the first term is the temporal change rate of  $M_k$ , the second term is the moment change rate caused by convection in physical space, and the third term is the moment change rate caused by positive or negative growth of the droplets, such as evaporation and condensation.

According to the relationship between the velocity  $\mathbf{U}(d)$  and the internal coordinate  $d$ , some simplifications might be made to the convection term. Considering the fact that the droplets or particles adopted in the experimental studies have a relatively narrow size range, they can be regarded as moving with the same velocity. Then, the velocity is independent of the internal coordinate  $d$ , and it can be moved out of the integral. Therefore, Equation (8) becomes

$$\frac{\partial M_k}{\partial t} + \nabla \cdot (\mathbf{U}_d M_k) + \int_0^{+\infty} d^k \frac{\partial}{\partial d}(G(d)n(d)) dd = 0, \tag{9}$$

where  $\mathbf{U}_d$  is the droplet velocity independent of internal coordinate  $d$ . In this case, Equation (9) can be solved by being coupled with the TFM. The TFM provides Equation (9) with the dispersed phase velocity as  $\mathbf{U}_d$  and the interphase mass transfer rate to calculate  $G(d)$ . Meanwhile, the DSD obtained from (9) is used to provide the dispersed phase diameter to calculate the interphase models of TFM. The details of this coupled approach can be found in our previous work [52].

#### 2.4. Eulerian–Lagrangian Approach

Finally, the E-L approach is summarized. This approach represents the dispersed phase as individually tracked particles [55–57]. The motion of a particle, considering gravity and drag forces, is governed by the following equation:

$$m_p \frac{d\mathbf{U}_p}{dt} = \frac{\pi d_p^3}{6} (\rho_p - \rho_c) \mathbf{g} + \frac{C_d}{2} \frac{\pi d_p^2}{4} \rho_c |\mathbf{U}_p - \mathbf{U}_c| (\mathbf{U}_p - \mathbf{U}_c), \quad (10)$$

where  $m_p$  is the particle mass,  $\mathbf{U}_p$  is the particle velocity,  $d_p$  is the particle diameter,  $\rho_p$  and  $\rho_c$  are the densities of the particle and continuous phase, respectively, and  $C_d$  is the drag coefficient. Turbulent dispersion is modeled using a stochastic approach:

$$\mathbf{U}_c = \bar{\mathbf{U}}_c + \mathbf{U}'_c, \quad (11)$$

where  $\bar{\mathbf{U}}_c$  is the mean continuous phase velocity obtained by solving the N-S equations and  $\mathbf{U}'_c = \zeta \sqrt{2k_c/3}$  represents the turbulent fluctuating velocity, with  $k_c$  as the continuous phase turbulence kinetic energy and  $\zeta$  as a random unit direction vector. Furthermore, details of mass and energy conservation equations of the particle and relevant heat and mass transfer models can be found in [52,58].

The E-L approach tracks individual droplet properties, such as mass and velocity, offering detailed insights into droplet dynamics. However, it incurs higher computational costs compared to Eulerian approaches due to the need to solve the motion equation for each particle. While the Eulerian approach predicts average droplet behavior using mean diameters, it may be computationally more efficient and requires less post-processing.

#### 2.5. Implementation of the Numerical Methods

The open-source software OpenFOAM v2106 [59] is adopted in this study. The air phase is regarded as compressible to consider the effect of temperature changes and buoyancy. The solver for the PSPM is implemented by adding the scalar transport equation to *buoyantSimpleFoam* and *buoyantPimpleFoam* for steady and unsteady cases, respectively. The unsteady solver, *reactingTwoPhaseEulerFoam*, is adopted for the TFM. The solver for the TFM-PBE coupled approach has been implemented based on OpenFOAM v2106 and validated in our previous work [52]. For the E-L approach, the standard solver of OpenFOAM v2106, *reactingParcelFoam*, is adopted. The simulations are performed on the high-performance computing system of Politecnico di Torino (CPU: Intel Xeon Gold 6130, 2.10 GHz, 16 cores).

### 3. Analysis of the Test Cases and Results

#### 3.1. The Pseudo-Single-Phase Model for Tracer Gas

To systematically compare the Eulerian approaches with the E-L approach, the PSPM and the E-L approach were first adopted to investigate the transport of gaseous pollutants or small aerosols. In this study, we adopted the experiment conducted by Tian et al. [17] where carbon dioxide (CO<sub>2</sub>) acted as a tracer gas, simulating small respiratory droplets or

aerosols. This was to assess the performance of displacement ventilation (DV), stratum ventilation (SV), and mixing ventilation (MV) in a small office setting.

### 3.1.1. Case Description and Numerical Method

As shown in Figure 2, a small office with thermal isolation was used in the experiment, with dimensions of 4 m × 3.5 m × 3.5 m (length × width × height). The inlets for displacement ventilation (DV, 1.56 m × 0.355 m), stratum ventilation (SV, 0.19 m × 0.09 m), and mixing ventilation (MV, 0.19 m × 0.09 m) were located on the front wall ( $y = 3.5$  m). The exhaust line extended into the office via a square pipe. The ceiling featured three fluorescent lights, each rated at 72 W. The room contained a desk, a closet, a computer (with the system unit on the floor and the monitor on the desk), and a manikin represented by a rectangular cuboid. A 100 W light bulb placed inside the manikin simulated the thermal effects of a sedentary human body, while the system unit operated at a power rate of 180 W. Various CO<sub>2</sub> emission points were evaluated during the experiment, including the floor ( $z = 0$  m), desk ( $z = 0.8$  m), and armpit ( $z = 1.0$  m). Measurements of velocity (ms<sup>-1</sup>), temperature (°C), and CO<sub>2</sub> concentration (parts-per-million, ppm) were recorded along vertical sampling lines under steady-state conditions.

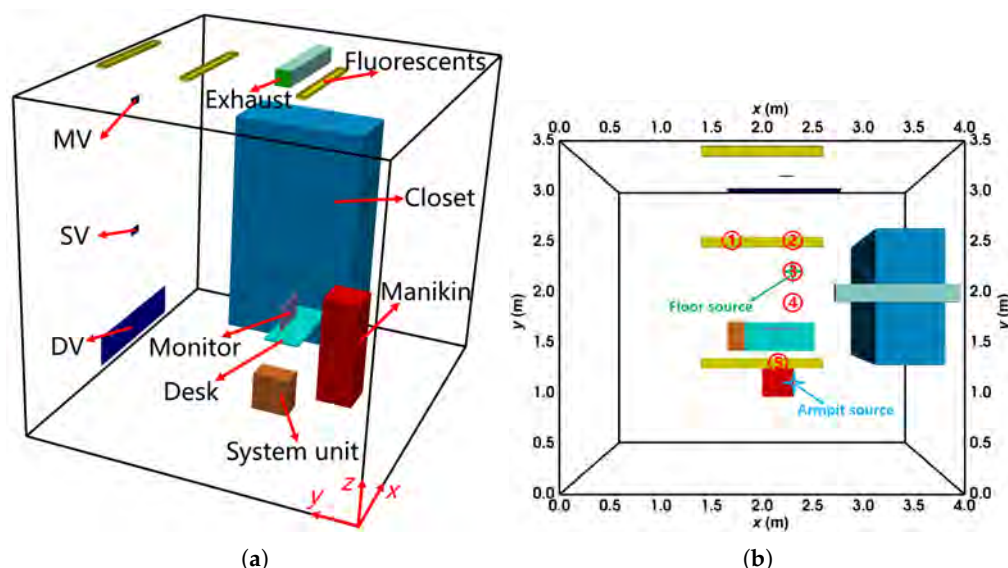


**Figure 2.** The configuration of the office with DV, SV, and MV: (a) the layout from the oblique view; (b) the locations of the vertical sampling lines and sources from the top view. The locations of sampling line 1 to 5 are  $(x, y) = (1.7, 2.5)$  m,  $(2.35, 2.5)$  m,  $(2.35, 2.2)$  m,  $(2.35, 1.9)$  m,  $(2.18, 1.25)$  m, respectively. The floor source location is  $(x, y, z) = (2.35, 2.20, 0.00)$  m, and the armpit source is  $(2.40, 0.95, 1.00)$  m.

The computational geometry was designed to replicate the experimental configuration, with simplifications made to reduce computational complexity. Features such as desk legs, keyboards, computer cables, and detailed structures of ventilation inlet diffusers were omitted. For example, the perforated diffuser at the DV inlet, with a perforated area ratio of 33.2%, was simplified as a uniform opening. To ensure consistency in supplied air momentum and flow rate, the method proposed by Zhang et al. [60] was adopted. This involved specifying the measured velocity for a subset of grid cells proportional to the perforated area ratio. This approach is widely used to simplify diffuser representations while maintaining accuracy in airflow simulations [22,61].

The other boundary conditions were specified according to the experimental setups. Six simulations were conducted for three ventilation systems under a single inlet flow rate (2.2 air changes per hour) and the source locations corresponding to floor (F) and

armpit (A). The case numbers corresponding to the experimental configurations were DV-A1, SV-A1, MV-A1, DV-F1, SV-F1, and MV-F1. Velocity values were assigned as previously described. No-slip boundary conditions were applied to walls and other surfaces, while a fixed pressure was set at the exhaust. For temperature, fixed temperatures or power ratings were applied to the inlet, fluorescents, system unit, and manikin. To reflect thermal isolation in the experiment, walls, and the ceiling were treated as adiabatic, while a fixed temperature was imposed on the floor. Additionally, inlet concentrations and CO<sub>2</sub> release rates were defined based on experimental data. The detailed boundary conditions are listed in Tables A1 and A2 in Appendix B.

The PSPM was adopted, modeling the air as a mixture of dry air, water vapor, and CO<sub>2</sub>, as relative humidity (RH) was measured in the experiment. Two species transport equations were solved for water vapor and CO<sub>2</sub>. The thermophysical properties were modeled as functions of temperature and composition, following the approach in Feng et al. [52]. The RNG  $k - \epsilon$  turbulence model [62] has demonstrated excellent accuracy in simulating indoor airflow [63,64]. Consequently, it was employed to model the continuous air phase throughout this study. Additionally, second-order discretization schemes were applied to the governing equations.

For comparison, the E-L approach was also adopted. Particles with a diameter of 1  $\mu\text{m}$  were released at the CO<sub>2</sub> source (armpit) at a rate of 1000 per second, mimicking CO<sub>2</sub> behavior. Drag and gravity forces were considered, with turbulent dispersion modeled through a stochastic tracking method. The RNG  $k - \epsilon$  turbulence model was similarly applied. Escape boundary conditions were set at the outlet, while rebound boundary conditions were used for walls and surfaces.

A hexahedral grid refined near walls and surfaces was built. Grid convergence was examined using three levels of refinement (258,232 cells for coarse, 553,632 for medium, and 1,222,930 for fine). Results from the medium and fine grids were very close and showed good consistency, leading to the adoption of the medium grid for simulations. Further details are provided in Appendix A.1.

### 3.1.2. Results and Discussion of Tracer Gas

Figures 3–5 present the predicted and measured profiles of velocity, temperature, and CO<sub>2</sub> concentration for DV, SV, and MV, respectively. The predicted results show good agreement with experimental data in most cases. Furthermore, the numerical simulations capture certain flow features that the experiments missed due to a limited number of measurement points. These findings confirm the reliability of the PSPM for modeling tracer gas transmission in indoor environments and its ability to provide detailed insights into airflow fields. Additionally, the different ventilation systems result in varying indoor airflow patterns, which influence the temperature, velocity, and CO<sub>2</sub> concentration profiles. These differences arise from the specific configuration of each system, including the location of inlets and exhausts, the cross-sectional area for air passage, and the air supply velocity. Such variations naturally lead to distinct airflow structures within the indoor environment, which, in turn, determine the effectiveness of each system in removing respiratory droplets. Figure 6 illustrates the velocity fields of DV, SV, and MV in the ( $x = 2.2\text{ m}$ ) plane, capturing the characteristic airflow patterns of each system as reported in [65]. A detailed discussion of these patterns and their implications is provided below.

For the case of DV, fresh cool air is supplied at a relatively low velocity from the lower part of the front wall, as shown in Figure 2a. Consequently, both the predicted and measured velocities are higher in the lower part of the room, as illustrated in Figure 3a. Similarly, Figure 3b shows that temperatures at the sampling lines are lower near the floor, where cool air is supplied, and higher near the ceiling due to the thermal effect of the fluorescents

(detailed temperature distribution is shown in Figure S1a of the Supplementary Material). Figure 6a further illustrates the velocity field in the  $x = 2.2$  m plane, intersecting the manikin and desk. The supplied cool air, having a higher density, initially moves downward due to gravity and then flows along the floor. Meanwhile, the thermal effect of the manikin creates upward buoyant airflow, particularly above the manikin’s head, which transports tracer gas or aerosols from the floor to the ceiling. When the CO<sub>2</sub> source is at the armpit, as shown in Figure 3c, the CO<sub>2</sub> concentration increases with height. When the source is on the floor, as shown in Figure 3d, the CO<sub>2</sub> concentration near the floor is particularly high at Locations 3, 4, and 5 because they are close to the floor source. Above this region, the CO<sub>2</sub> concentration also increases with height. These results indicate that DV effectively transports gaseous pollutants or small droplets upward, reducing the risk of indoor infection.

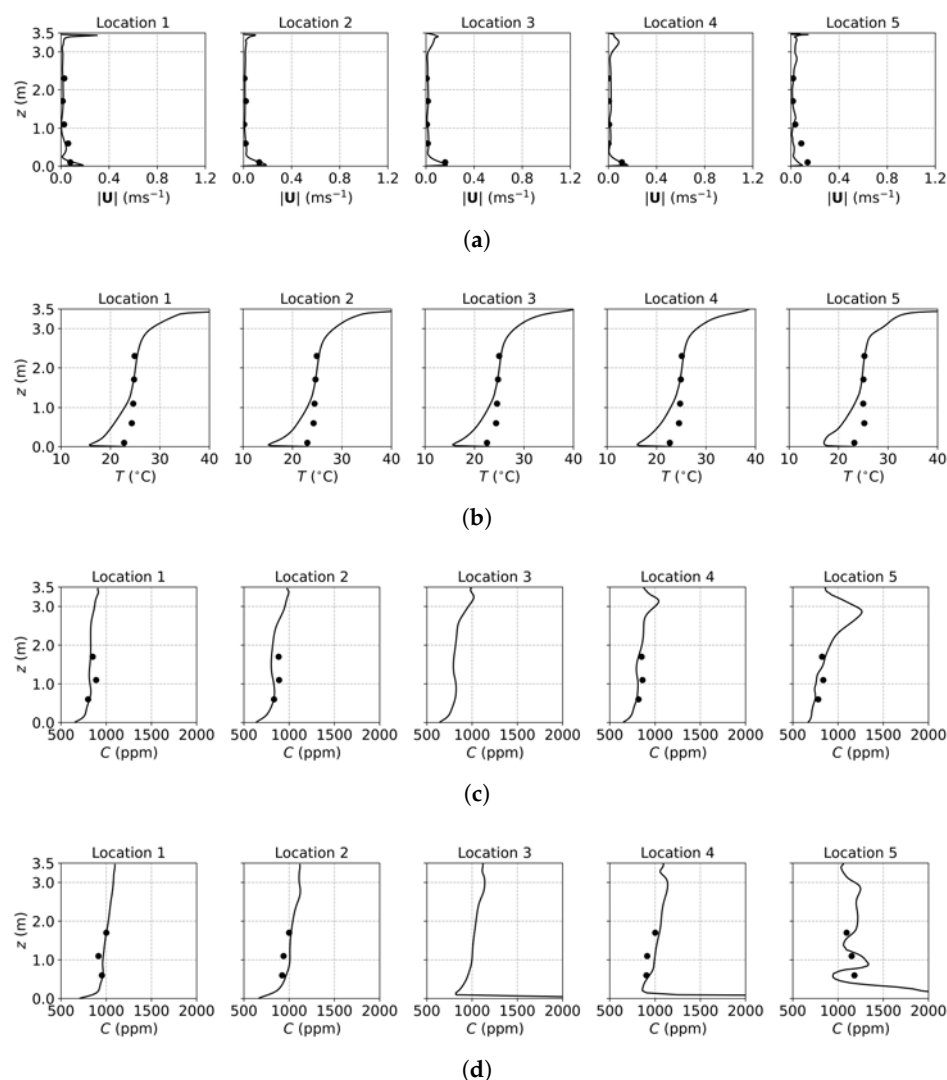


**Figure 3.** The predicted and measured results along the sampling lines under DV: (a) velocity magnitude; (b) temperature; (c) CO<sub>2</sub> concentration with source located at the armpit ( $z = 1.0$  m); (d) CO<sub>2</sub> concentration with source located on the floor ( $z = 0$  m). Circles: experimental data [17]; solid lines: numerical results of the PSPM.

For the case of SV, fresh cool air is supplied from the middle part of the front wall, as shown in Figure 2a. Operating under the same air change rate, its velocity is higher than that of DV due to the smaller inlet size. As shown in Figure 4a, at Locations 2, 3, 4, and 5, both predicted and measured velocities exhibit significant peaks at the injection height,

which decrease with increasing distance from the inlet (from Location 2 to Location 5). At Location 1, far from the SV inlet, no such peak is observed, and the velocity is small and relatively uniform. Figure 4b shows the temperature profiles. Similar to the velocity profiles, the numerical results indicate low-temperature peaks at the injection height due to the supplied cool air. These peaks are not captured in the experimental results because of the limited number of measurement points (the temperature contour can be found in Figure S1b of the Supplementary Material). Figure 6b illustrates the velocity field under SV, revealing that the supplied air impinges on the manikin. Most of the airflow moves downward along the front surface of the manikin, continues along the floor and the front wall, and forms a large recirculation region in front of the manikin in the lower part of the office. A smaller portion of the airflow passes above the manikin’s head, impinges on the back wall, and creates a recirculation region behind the manikin. Additionally, the obstruction of the monitor causes a part of the airflow to move downward along its surface. These airflow patterns determine the distribution of CO<sub>2</sub> in the office.

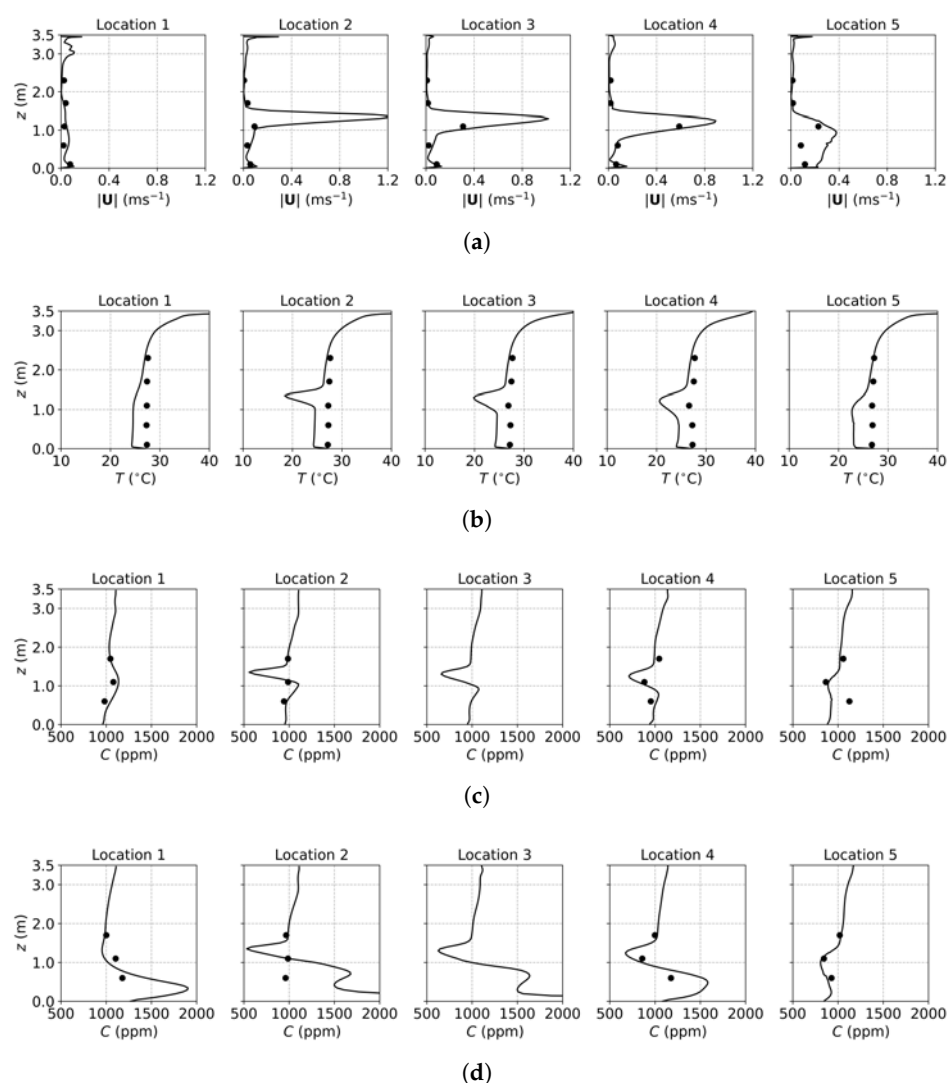


**Figure 4.** The predicted and measured results along the sampling lines under SV: (a) velocity magnitude; (b) temperature; (c) CO<sub>2</sub> concentration with source located at the armpit ( $z = 1.0$  m); (d) CO<sub>2</sub> concentration with source located on the floor ( $z = 0$  m). Circles: experimental data [17]; solid lines: numerical results of the PSPM.

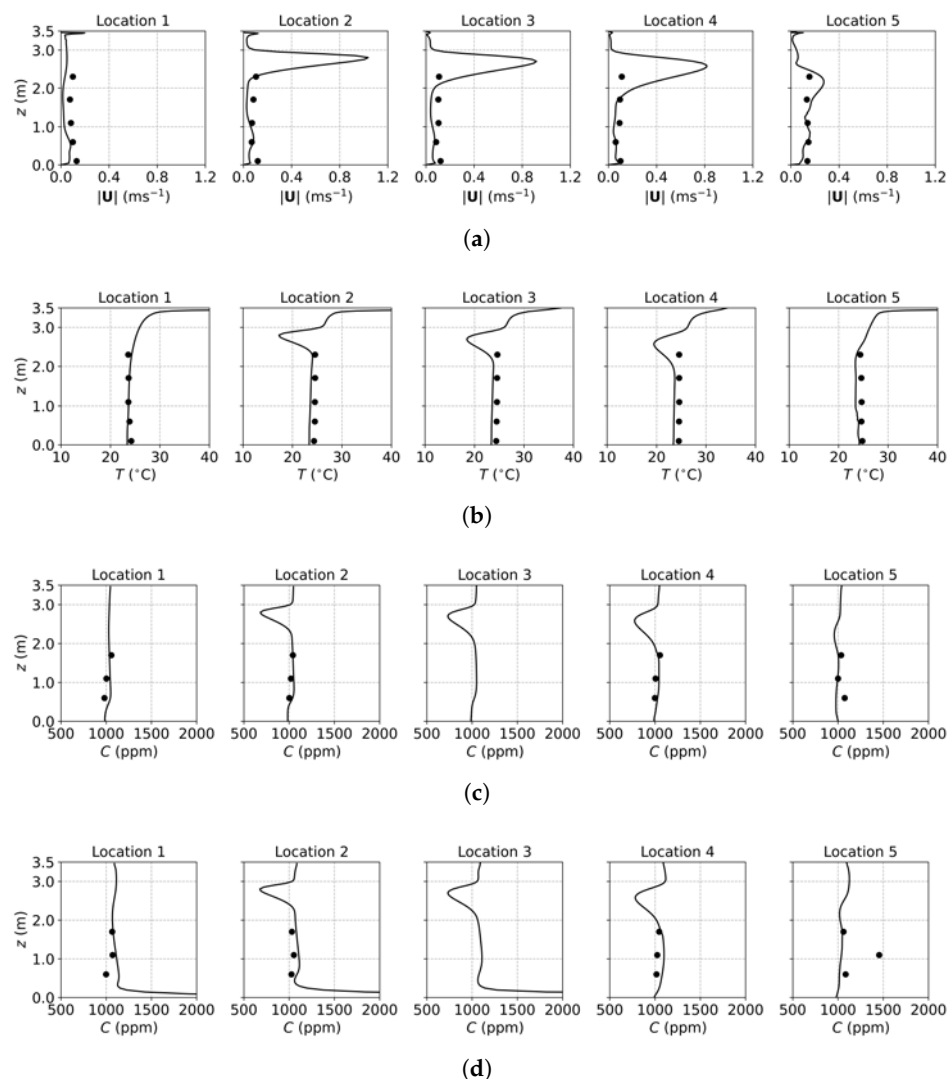


**Figure 5.** The predicted and measured results along the sampling lines under MV: (a) velocity magnitude; (b) temperature; (c) CO<sub>2</sub> concentration with source located at the armpit ( $z = 1.0$  m); (d) CO<sub>2</sub> concentration with source located on the floor ( $z = 0$  m). Circles: experimental data [17]; solid lines: numerical results of the PSPM.

Figure 4c presents the CO<sub>2</sub> concentration profiles when the source is located at the armpit ( $z = 1.0$  m). At Location 2, a distinct low-concentration peak is observed at the height of the SV injection, caused by the fresh air directly passing through the sampling line. Below this peak, a smaller high-concentration region appears due to the recirculation in front of the manikin. Downstream, at Locations 3 to 5, the CO<sub>2</sub> concentration profiles exhibit similar shapes but with progressively diminishing peaks, reflecting the interaction with the surrounding air. At Location 1, distant from the SV inlet, no low-concentration peak is observed; instead, a small high-concentration peak appears due to recirculation. When the CO<sub>2</sub> source is on the floor ( $z = 0$  m), as shown in Figure 4d, similar low-concentration peaks are observed at Locations 2 to 5, while higher concentrations persist near the floor. This is attributed to the CO<sub>2</sub> source being situated within the recirculation region near the manikin, which hinders CO<sub>2</sub> transport to other regions.

The SV system, which supplies fresh air directly to the breathing zone in front of the manikin, significantly reduces infection risk by minimizing exposure to contaminated air. However, its effectiveness can be easily influenced by the positioning of occupants and the arrangement of furniture. For instance, a standing person may find it challenging to benefit from the injected fresh air, while a larger monitor or physical barriers could obstruct the SV

airflow, diminishing its performance. Therefore, careful consideration of indoor layout and occupant positioning is crucial to optimize the effectiveness of SV systems.

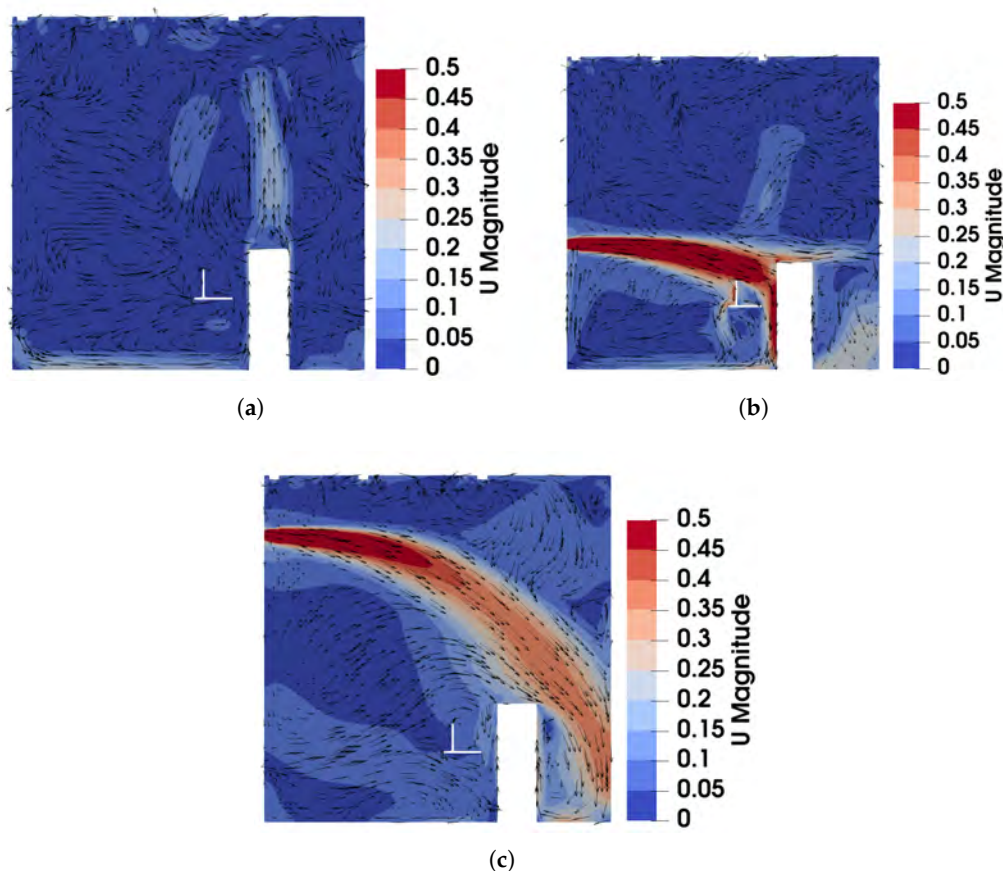


**Figure 6.** The velocity field of DV, SV, and MV in the plane of  $x = 2.2$  m: (a) DV; (b) SV; (c) MV.

For the case of MV, fresh cool air is supplied from the upper part of the front wall, as shown in Figure 2a. Similar to SV, the air velocity is relatively high due to the smaller inlet size compared to DV. As shown in Figure 5a, numerical results exhibit pronounced velocity peaks at the injection height (upper part of the office) at Locations 2, 3, 4, and 5, with a uniform velocity profile below the injection height. Correspondingly, the temperature profiles in Figure 5b display low-temperature peaks at the injection height, while the temperature remains nearly uniform below this level (also in Figure S1c of the Supplementary Material). Figure 6c shows the velocity field under MV, showing that the injected airflow descends gradually due to gravity, forming recirculation regions that mix the indoor air. These recirculations create a uniform environment in terms of both temperature and CO<sub>2</sub> concentration. As a result, below the injection height, CO<sub>2</sub> concentrations are uniform for both source locations, as shown in Figure 5c,d. While MV effectively reduces the total amount of aerosols, it promotes uniform dispersion, which might not be suitable for infection control as it can spread infectious particles evenly throughout the room.

Since the flow fields of the background airflow are mainly governed by the ventilation systems and are less affected by the gaseous pollutants or small-size aerosols, the E-L approach gives velocity and temperature fields close to the PSPM. For the sake of conciseness, only concentration distributions from the E-L approach are presented, as shown in Figure 7. Particles are released only at the CO<sub>2</sub> source, excluding those from the ventilation inlet and initial background. Since the E-L approach used particles to represent CO<sub>2</sub> gas, scaling from particle number to CO<sub>2</sub> mass fraction may introduce some deviations. As a result, comparing the transport trends rather than the concentration values is more

reasonable for the E-L approach. The transport trends for the three ventilation systems align with those obtained using the PSPM. Under DV, particle concentration increases with height due to upward buoyant flows, while SV creates a low-concentration region at the breathing zone. MV, on the other hand, provides a relatively uniform distribution. However, the concentration profiles in the E-L simulations are less smooth compared to the PSPM results. This discrepancy arises from the stochastic tracking model, which may underpredict turbulent dispersion, particularly under SV and MV with higher turbulence intensities. The underpredicted turbulent dispersion of particles results in less uniform particle distributions under SV and MV. Additionally, the particle source in-cell scheme [66] used for post-processing converts the discrete particle distribution into concentration profiles. This approach requires a balance: the concentration mesh must be large enough to include sufficient particles for statistical reliability but small enough to preserve local details. Consequently, the post-processed results are only statistically smooth. This problem may be mitigated by increasing the number of tracked particles. Finally, computational costs are compared using DV as an example. For 1000 time steps on a single CPU core, the PSPM and E-L approaches require 1.68 h and 2.71 h, respectively, with the E-L approach incurring 61% higher computational costs since computing particle trajectories requires the solution of additional equations.

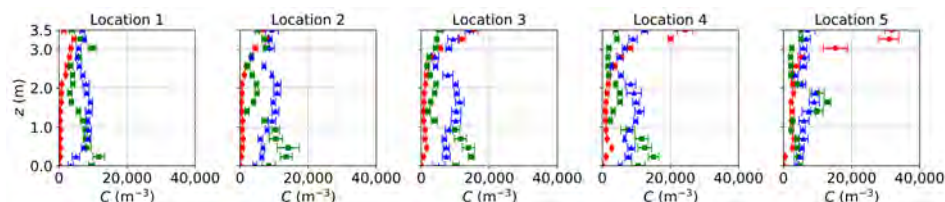


**Figure 7.** Concentration distributions along the sampling lines under DV, SV, and MV obtained using the E-L approach. The particle source is located at the armpit ( $z = 1.0$  m). Red circles: DV; green squares: SV; blue triangles: MV. The error bar represents the standard deviation of time averaging.

In summary, the velocity, temperature, and  $\text{CO}_2$  concentration profiles obtained using the PSPM show good agreement with experimental data. While the E-L approach effectively captures the transport trends of different ventilation systems, it requires higher computational costs and additional post-processing effort. Furthermore, the DV, SV, and MV systems exhibit distinct indoor airflow patterns, resulting in varying performances for infection control.

### 3.2. The Two-Fluid Model for Particles

The TFM was utilized to simulate particle transport in indoor ventilation systems, with results compared to the E-L approach. The study employed experimental data from Liu et al. [22], which measured velocity, temperature, and tracer particle concentrations in a large office ventilated by DV and MV.

#### 3.2.1. Case Description and Numerical Method

As shown in Figure 8a, the office dimensions were  $7 \text{ m} \times 5.8 \text{ m} \times 3.05 \text{ m}$  (length  $\times$  width  $\times$  height). The DV inlet was located on the left wall ( $x = 0 \text{ m}$ ), two MV inlets were on the ceiling, and the exhaust was in the corner of the ceiling. The office contained four manikins (A, B, C, and D), four desks, four chairs, and four computers (including system units and monitors). Each manikin was heated to simulate human thermal effects, producing approximately 80 W of heat. Additional features included a TV on the front wall ( $y = 5.8 \text{ m}$ ), a table in the corner, and ten 64 W fluorescent lights on the ceiling. Solid droplet residues, ranging in size from  $0.3 \mu\text{m}$  to  $2 \mu\text{m}$ , were used as tracer particles and injected from the mouth of Manikin A at a velocity of  $1.58 \text{ ms}^{-1}$ , in cycles

of 0.8 s on and 1.2 s off. During the experiment, profiles of velocity ( $\text{ms}^{-1}$ ), temperature ( $^{\circ}\text{C}$ ), and particle concentration ( $\text{m}^{-3}$ ) were measured along four vertical sampling lines, as shown in Figure 8b. Additionally, the temperatures of heated surfaces were measured to define boundary conditions for the simulations.

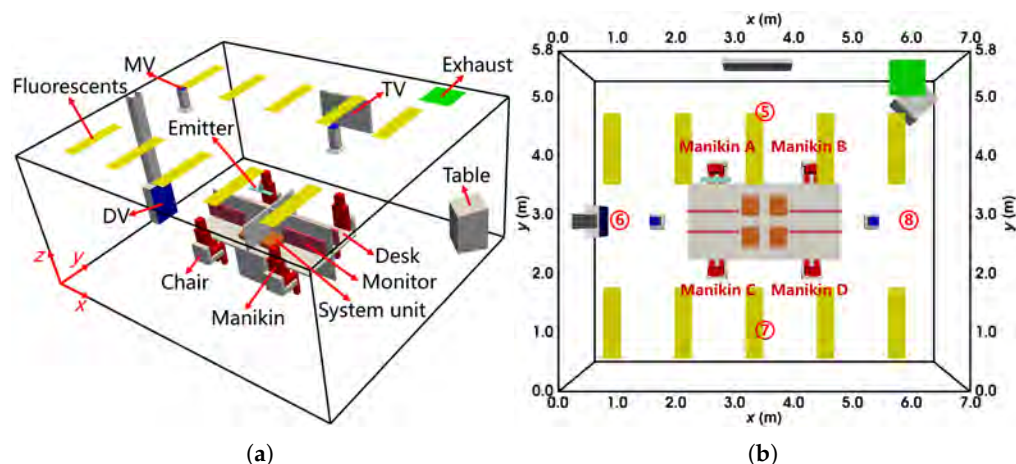


**Figure 8.** The configuration of the office with DV and MV: (a) the layout from the oblique view; (b) the locations of sampling lines from the top view. The locations of sampling line 5 to 8 are  $(x, y) = (3.5 \text{ m}, 4.8 \text{ m}), (1.0 \text{ m}, 2.9 \text{ m}), (3.5 \text{ m}, 1.0 \text{ m}), (6.0 \text{ m}, 2.9 \text{ m})$ , respectively.

Compared to the experimental configuration, several simplifications were made to model the geometry. Keyboards and computer cables were omitted, while manikins and chairs were approximated using cuboids of similar dimensions as shown in Figure 8a. The DV diffuser was simplified as in Section 3.1, whereas the MV inlet geometry was modeled as in the experiment. Additionally, round pipes in the ventilation system were replaced with square pipes. These simplifications significantly reduced grid complexity and the number of cells while maintaining reasonable accuracy, as demonstrated by the results presented later.

The experimental setups, with a supplied air flow rate of 4 air changes per hour (ACH), were adopted for the simulations. For DV, a diffuser perforated area ratio of 20% was used to calculate the inlet velocity, determined following the method of Zhang et al. [60], as described in Section 3.1. For MV, a uniform inlet velocity corresponding to 4 ACH was applied to the two inlets. Temperature boundary conditions for walls and surfaces were derived from experimental measurements, while adiabatic conditions were assigned to surfaces without specified temperatures [22]. Fixed-temperature boundary conditions for the fluorescents were set to match their power ratings. The particle emitter velocity was prescribed as a constant  $1.58 \text{ ms}^{-1}$ , consistent with the simulations of Liu et al. [22], and the particle volume fraction was set to  $1 \times 10^{-6}$ . Further detailed boundary conditions can be found in Tables A3 and A4 in Appendix B.

The TFM was adopted for transient simulations of particle transmission, treating both air and particles as continua with two sets of N-S equations solved for the phases. The diameter of the dispersed phase was set to  $0.4 \mu\text{m}$ , as the experiment focused on particles of this size. This small particle size ensures sufficient particles within each grid cell for the continuum assumption to hold, given a volume fraction of approximately  $1 \times 10^{-6}$  [53]. Moreover, the Stokes number (St) satisfies the requirements for applying the TFM, as discussed below. For interphase interactions, only drag force and heat transfer were considered, with the former modeled using the Schiller and Naumann approach and the latter calculated via the Ranz–Marshall correlation [52]. The RNG  $k - \epsilon$  turbulence model was applied to the continuous air phase, while the dispersed particle phase was assumed to be laminar. The continuous phase was modeled as a perfect gas with temperature-

dependent thermophysical properties, while constant properties were assigned to the dispersed phase. Second-order schemes were used for the discretization of the governing equations. The PSPM and E-L approaches were also implemented for comparison, using setups consistent with the previous case.

The simulations were conducted using hexahedral grids refined near walls, surfaces, and the particle emitter region. Grid convergence was tested with three grid levels: coarse (964,947 cells), medium (1,965,986 cells), and fine (4,571,857 cells). The medium grid (1,965,986 cells) showed consistent results with the fine grid, making it the optimal choice for this study. Details are provided in Appendix A.2. To further reduce computational costs, the MV inlet geometries were omitted in the DV simulations.

### 3.2.2. Results and Discussion of Non-Evaporating Particles

Figure 9 presents the air velocity, air temperature, and normalized particle concentration profiles under DV obtained from experimental measurements [22], PSPM, TFM, and the E-L approach. Figure 9a shows the air velocity magnitude, with all three numerical approaches producing results close to the experimental data. Due to the DV system supplying fresh cool air near the floor, higher velocities are observed close to the ground, particularly at Location 6, which is nearest to the DV inlet, as shown in Figure 8b. Figure 9b depicts the temperature profiles, where numerical predictions align well with the measurements. Cooler temperatures near the floor reflect the influence of the fresh air supply, while higher temperatures in the upper regions are due to the thermal effects of heat sources such as manikins and fluorescent lights (the detailed temperature distribution can be found in Figure S2a,c of the Supplementary Material).

The normalized particle concentration,  $C^*$ , shown in Figure 9c, is defined as  $C^* = (C - C_s)/(C_e - C_s)$ , where  $C$ ,  $C_s$ , and  $C_e$  represent the particle concentration at a specific location, the supply, and the exhaust, respectively. The concentration profiles predicted by the three approaches are similar overall. At Locations 5 and 7, the agreement between predicted and measured profiles is excellent, with the TFM showing the closest match to the experimental data. The PSPM results are more diffusive compared to the other two approaches and underestimate the concentrations at Location 5, likely due to overestimated turbulent interaction using the default  $Sc_t = 0.7$ . The E-L approach achieves better agreement than the PSPM but requires additional post-processing to convert tracked particle data into concentration fields. At Locations 6 and 8, all three approaches underpredict the measured concentrations, consistent with findings from Liu et al. [22], who attributed the discrepancies to geometric and boundary condition simplifications.

Figure 10 presents the air velocity, air temperature, and normalized particle concentration profiles under MV. The results of the PSPM and TFM are close and agree well with the experimental data. While the E-L approach shows good agreement for velocity and temperature profiles, it deviates in concentration predictions, particularly at Location 6. MV supplies fresh air with a higher turbulent intensity and induces a stronger turbulent mixing in the office, which creates a uniform environment, as seen in Figure 10b,c (also in Figure S2b,d of the Supplementary Material). However, the stochastic tracking model used in the E-L approach underpredicts turbulent dispersion, leading to less uniform concentration profiles. To achieve more accurate E-L simulations, stochastic tracking models capable of accurately describing turbulent dispersion are required.

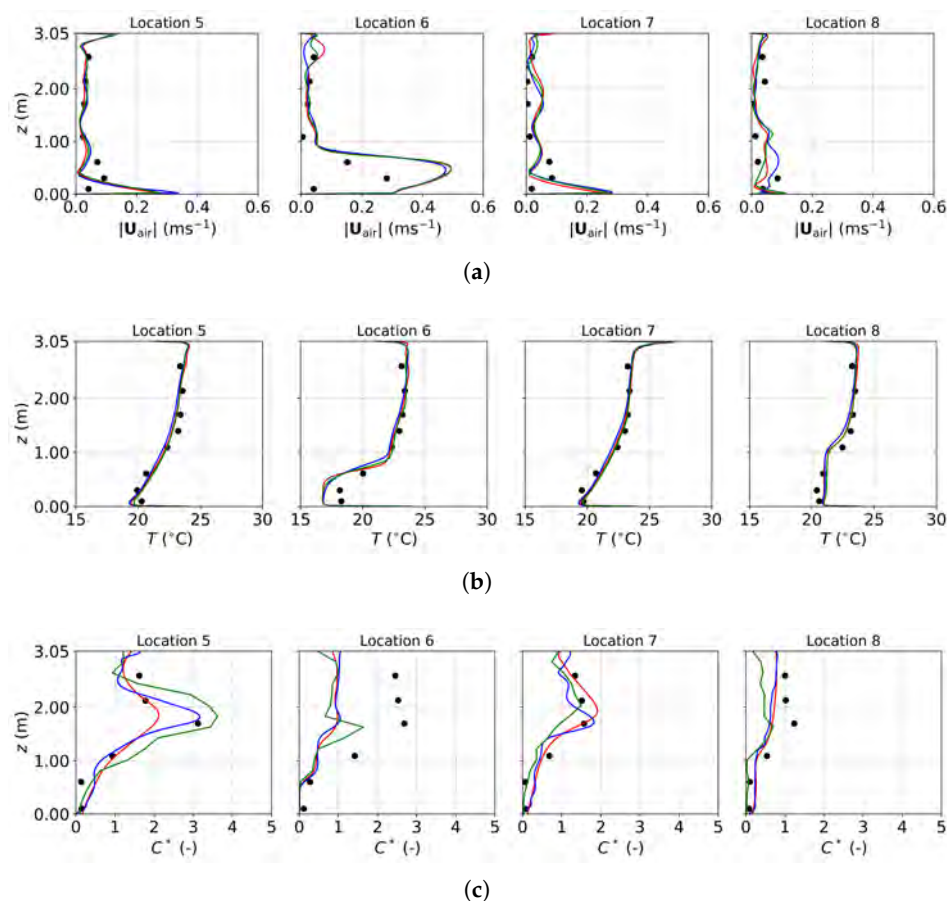


**Figure 9.** The predicted and measured results along the sampling lines under DV: (a) air velocity magnitude; (b) air temperature; (c) normalized particle concentration. Black circles: experimental data [22]; red lines: numerical results of the PSPM; blue lines: numerical results of the TFM; green lines: numerical results of the E-L approach.

Figure 11 shows the air and particle velocities obtained using the TFM in the  $x = 2.55$  m vertical plane, providing more comprehensive insights compared to velocity profiles alone. Comparing Figure 11a with Figure 11b or Figure 11c with Figure 11d, it is evident that the particle velocity closely matches the air velocity. To quantify this similarity, the relative difference between air and particle velocities is defined as  $D_{U_r} = |\mathbf{U}_{air} - \mathbf{U}_{particles}| / |\mathbf{U}_{air}|$ . For DV,  $D_{U_r}$  is less than 0.1% in most of the office and less than 1.0% throughout. Similarly, under MV,  $D_{U_r}$  remains below 0.1% in the entire office. These findings confirm that the particles effectively follow the airflow. For the particle size considered ( $0.4 \mu\text{m}$ ), the Stokes number ( $St$ ) is approximately  $1.94 \times 10^{-4}$  for DV and  $7.32 \times 10^{-4}$  for MV. The Stokes number is calculated as  $St = \tau_p / \tau_k$ , where  $\tau_p = \rho_p d_p^2 / (18\mu_c)$  is the particle relaxation time, and  $\tau_k = \sqrt{\nu_c / \epsilon_c}$  is the Kolmogorov time scale. According to Balachandar and Eaton [55], when  $St < 0.2$ , the PSPM can safely predict particle transport.

Under DV, as shown in Figure 11a, upward buoyant flows caused by thermal effects from the manikins and monitors dominate, while near the floor, high velocities are observed due to the low inlet location. In other regions of the office, airflow velocities remain relatively low, as there are no additional heat sources driving circulation. Conversely, under MV, as illustrated in Figure 11c, the injected high-speed cool air from the ceiling generates large recirculation regions around the manikins and furniture. These recirculations, combined with buoyant flows similar to those under DV, result in higher overall air velocities, ultimately achieving a thorough mixing of the indoor air and a uniform environment.

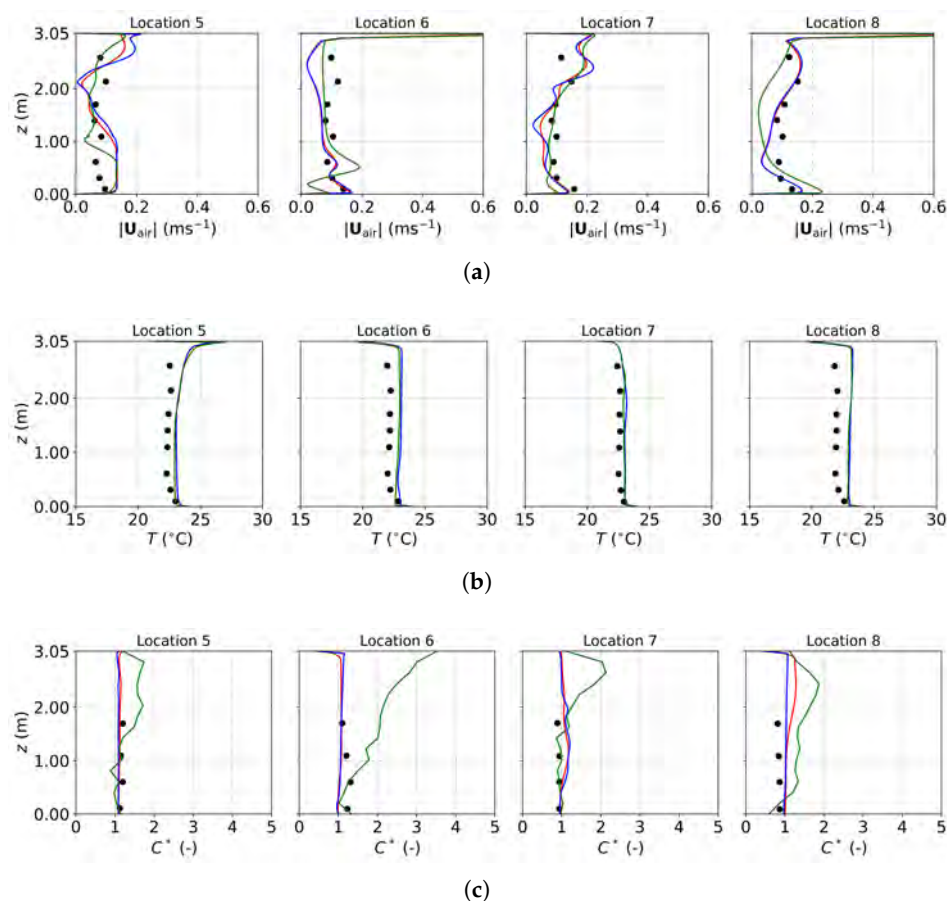


**Figure 10.** The predicted and measured results along the sampling lines under MV: (a) air velocity magnitude; (b) air temperature; (c) normalized particle concentration. Circles: experimental data [22]; red lines: numerical results of the PSPM; blue lines: numerical results of the TFM; green lines: numerical results of the E-L approach.

Figure 12 shows the velocity and normalized particle concentration distributions in the horizontal plane at  $z = 1.12$  m, corresponding to the height of the particle emitter outlet center. Under DV, as illustrated in Figure 12a, the velocity is high only near the particle emitter and heated surfaces, such as manikins and monitors. In the right part of the office, the airflow is directed leftward due to recirculations caused by interactions between the supplied air and buoyant flows. The supplied air flows along the floor, turns upward near the right wall ( $x = 7$  m), and combines with buoyant flows that ascend, move along the ceiling, and descend again near the right wall, creating a leftward flow. Figure 12b shows the normalized particle concentration ( $C^*$ ) distribution. Under DV, particles injected into the office are transported by recirculating buoyant airflows to areas behind Manikin A and C before dispersing throughout the office. Due to barriers and leftward flows, particles rarely reach the right side of the office, creating a relatively low infection risk for Manikin B and D.

Figure 12c shows the velocity distribution under MV. The airflows are more complex than those under DV, featuring recirculations driven by buoyant flows and the supplied air. These recirculations enhance indoor air mixing, resulting in an almost uniform dispersion of particles throughout the office, as shown in Figure 12d. Furthermore, Table 1 compares the number and average age of particles remaining in the office at  $t = 500$  s. DV retains fewer particles with a lower average age than MV, indicating that DV is more effective at particle removal. Consequently, DV appears to be a better option than MV for controlling indoor infection risks.

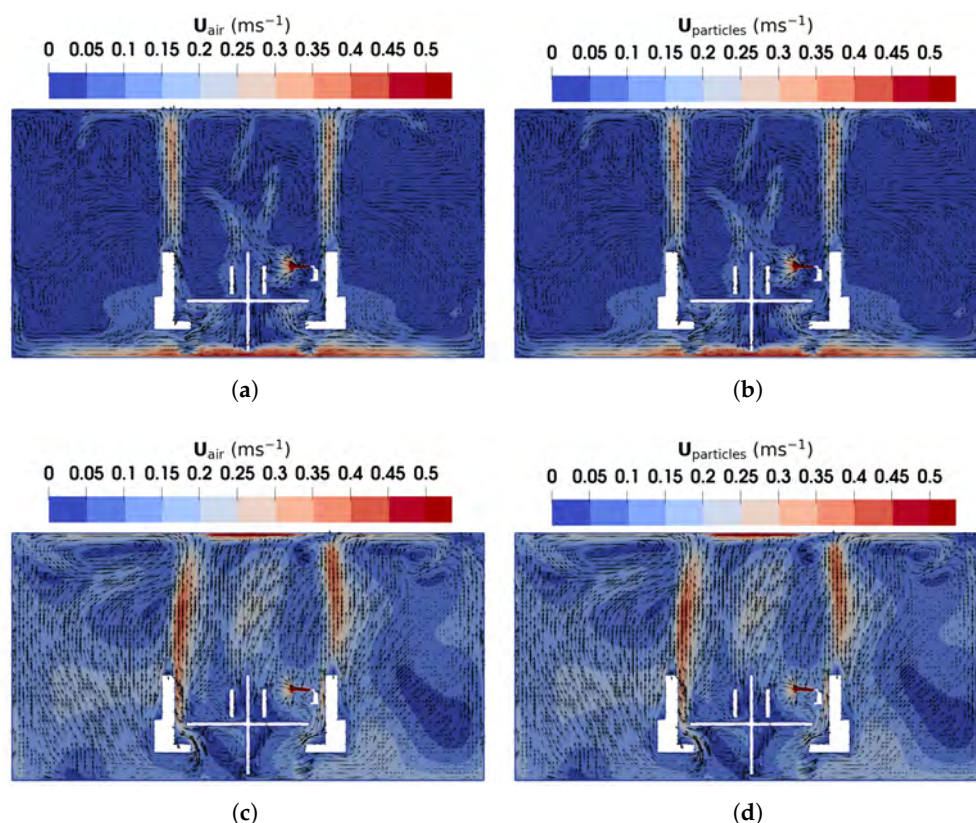


**Figure 11.** The magnitude and direction of air and particles velocity obtained using TFM in the vertical plane of  $x = 2.55$  m: (a) air velocity under DV; (b) particles velocity under DV; (c) air velocity under MV; (d) particles velocity under MV.

**Table 1.** Particle number and velocity at  $t = 500$  s.

Variables	DV	MV
Total particle number (-)	1,000,000	1,000,000
Active particle number (-) <sup>1</sup>	759,987	877,232
Maximum particle velocity ( $\text{ms}^{-1}$ )	1.57	2.36
Average particle velocity ( $\text{ms}^{-1}$ )	0.15	0.13
Particle number for $U_p > 0.4 \text{ ms}^{-1}$ (-) <sup>2</sup>	212,791	107,010
Average age of active particles (s)	221.32	235.75

<sup>1</sup> The active particles are those remaining in the computing domain. <sup>2</sup> The threshold value  $0.4 \text{ ms}^{-1}$  is estimated using the grid cell volume, the time step, and the Courant number. Particles with a velocity larger than this value may require sub-time step iterations to avoid the Courant number exceeding one.

Finally, the computing times of the three numerical approaches, as shown in Table 2, are discussed. The computing time of the PSPM is the smallest because it solves the N-S equations and only one additional scalar transport equation. The TFM solves two sets of N-S equations. Therefore, its computing time is about 2.5 times that of PSPM. For the E-L approach, tracing the transport of a huge number of particles significantly increases the computational costs and results in the highest computing time. For the PSPM and TFM, the computing time for MV is larger than that of DV because MV has more grid cells, as mentioned before. For the E-L approach, the computing time for MV, however, is smaller than that of DV. This may originate from the differences in particle velocities. To accurately trace the trajectories of the particles, the time step for a high-speed particle will be divided into several sub-time steps to avoid having too large of a particle Courant number. As shown in Table 1, though the case of DV has fewer grid cells and active particles, it has more particles with a higher velocity than the case of MV. These particles require

more sub-time-step iterations and thus result in higher computing time. The computing time also depends on the time step and the simulation time. In this study, the TFM adopted a smaller time step (0.001 s) than the E-L approach (0.01 s) to avoid numerical instability. The E-L approach requires a longer simulation time to inject enough particles for a reliable result. Therefore, the total computing times of the two approaches for the current cases are similar.

**Table 2.** Average computing time for every 1000 time steps using 16 CPU cores.

Approach	DV (h)	MV (h)
PSPM	0.51	0.65
TFM	1.36	1.64
E-L	1.86	1.80

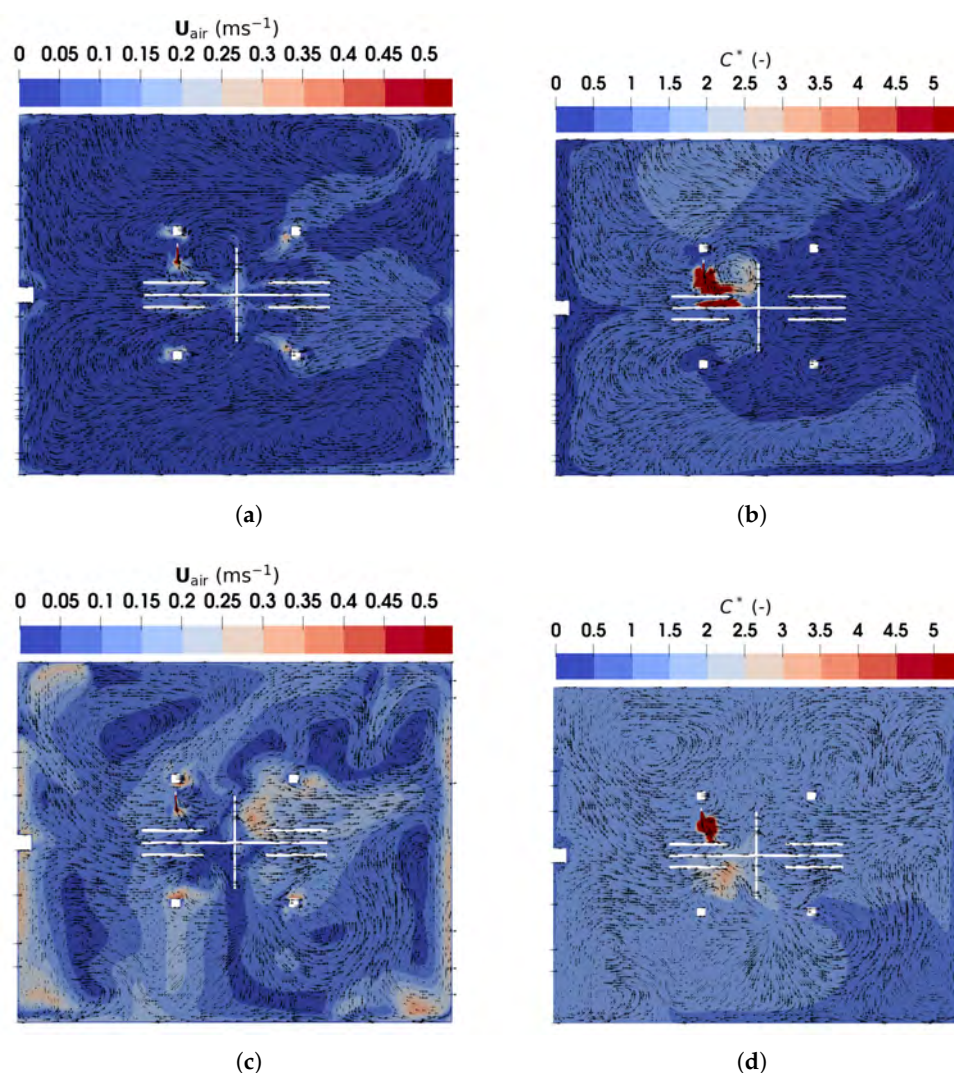


**Figure 12.** The magnitude and direction of air and particle velocity obtained using TFM in the horizontal plane of  $z = 1.12$  m: (a) air velocity under DV; (b) normalized particle concentration under DV; (c) air velocity under MV; (d) normalized particle concentration under MV.

In summary, the TFM accurately predicts particle transmission within a narrow size range in ventilated environments. The PSPM tends to overestimate turbulent dispersion under DV, while the E-L approach underestimates it under MV. Depending on the chosen time step and simulation duration, the computational costs of the TFM are smaller than or comparable to those of the E-L approach.

### 3.3. The TFM-PBE Coupled Approach for Evaporating Droplets

The TFM-PBE coupled approach was employed to model the transmission and evaporation of respiratory droplets. Data from the experiment by Wang et al. [25], which measured the concentration and size distribution of evaporating droplets in a negative pressure isolation ward with MV, were used for comparison and validation.

#### 3.3.1. Case Description and Numerical Method

The dimensions of the ward, shown in Figure 13a, are 4.22 m × 2.66 m × 2.8 m (length × width × height). Two ceiling-mounted MV inlets, each 0.135 m × 0.24 m, supply air, while the exhaust, sized 0.27 m × 0.27 m, is located in the lower corner. The ward contains one manikin, a bed, a table, and an equipment belt above the bed. The manikin was heated to maintain a temperature of 34 ± 1 °C. In the simulations, the manikin geometry was simplified to cuboids with similar dimensions. Additionally, two door gaps in the back wall (y = 0 m) facilitated air exchange due to pressure differences: door gap 1 (1.14 m × 0.02 m) allowed airflow into the ward at 2 ms<sup>-1</sup>, and door gap 2 (0.9 m × 0.02 m) allowed airflow out at 2.3 ms<sup>-1</sup>.

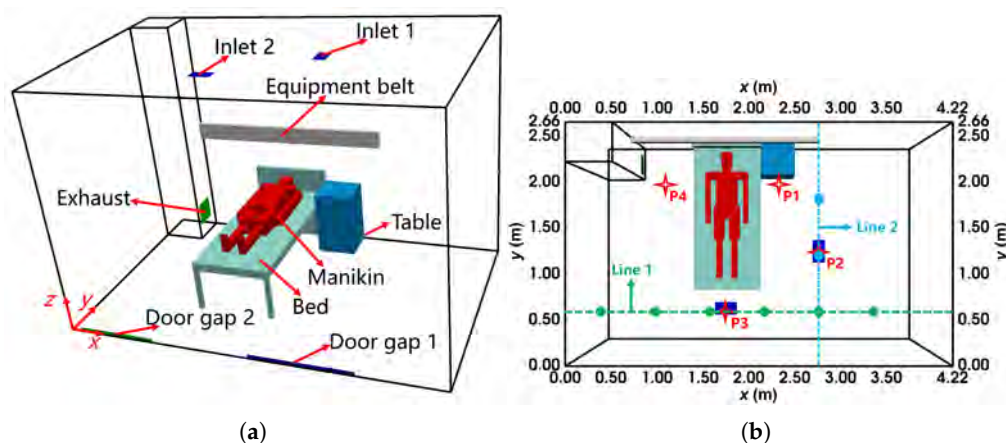


**Figure 13.** The configuration of the negative pressure isolation ward with MV: (a) the layout from the oblique view; (b) the locations of sampling lines and points from the top view. The location of velocity sampling line 1 is (y, z) = (0.6 m, 1.5 m) while the location of line 2 is (x, z) = (2.8 m, 1.5 m). The locations of concentration and size distribution sampling points 1 to 4 are (x, y, z) = (2.27 m, 1.96 m, 1.6 m), (2.76 m, 1.25 m, 1.6 m), (1.75 m, 0.6 m, 1.6 m), (1.1 m, 1.96 m, 1.6 m), respectively.

In the experiment, artificial saliva was used to generate evaporating tracer droplets, which were injected from the mouth of the manikin. Measurements indicated that droplet sizes ranged from 0.3 μm to 5 μm. As shown in Figure 13b, velocity profiles (ms<sup>-1</sup>) were measured along two horizontal sampling lines, while droplet concentration (m<sup>-3</sup>) and size distribution were measured at four sampling points.

The boundary conditions were defined based on the experimental setups. A fixed velocity at the two MV inlets ensured an air flow rate of 12 ACH. At the door gaps, the experimentally measured velocity magnitudes and directions were prescribed. No-slip velocity conditions were applied to walls and other surfaces, with a fixed pressure at the exhaust. The MV inlet temperatures were set to 299.1 K, while the manikin surface temperature was fixed at 307.1 K. Other walls and surfaces were treated as adiabatic. The ward RH was maintained at 60%. For the droplet emitter, the conditions modeled a breath: a velocity of 0.5 ms<sup>-1</sup>, a temperature of 309.1 K, and an RH of 90%. The droplet volume fraction was set at 1 × 10<sup>-6</sup>. Moments were computed using the measured size distribution at the emitter, which divided the droplet size range into ten intervals. The *i*th-order moment,  $M_i$ , was calculated as  $M_i = \sum_{j=1}^{10} k f_j d_j^i$ , where  $f_j$  represents the droplet percentage in the

$j$ th interval,  $d_j$  is its midpoint, and  $k = 6\alpha_d / (\pi \sum_{j=1}^{10} f_j d_j)$  ensures consistency with the dispersed phase volume fraction ( $\alpha_d = \pi M_3 / 6$ ). The inlet moments are summarized in Table 3. The Sauter mean diameter of the injected population of droplets, calculated using  $d_d = M_3 / M_2$ , was 2.25  $\mu\text{m}$ . Droplet deposition was excluded from consideration, as the focus of this study was on their evolution within the ward. Table A5 in Appendix B lists detailed boundary conditions.

**Table 3.** Moments at the inlet for the case of droplet transmission in the isolation ward.

$\alpha_d$ (-)	$M_0$ ( $\text{m}^{-3}$ )	$M_1$ ( $\text{m}^{-2}$ )	$M_2$ ( $\text{m}^{-1}$ )	$M_3$ (-)
$1 \times 10^{-6}$	$4.01305 \times 10^{11}$	$4.93606 \times 10^5$	$8.49231 \times 10^{-1}$	$1.90986 \times 10^{-6}$

Since the droplet sizes were distributed in a relatively narrow range, the coupled TFM-PBE approach was employed for transient simulations, treating droplets of various sizes as moving with the same velocity. The Schiller and Naumann drag force model, Ranz–Marshall heat transfer model, and Frossling mass transfer model were applied to describe interphase interactions. The RNG  $k - \epsilon$  turbulence model was used for the continuous phase, while the dispersed phase was treated as laminar. A temperature- and composition-dependent thermophysical property model was implemented [52]. For the PBE setup, two quadrature nodes were employed, solving four moment transport equations. To model droplet residues from the experiment, a minimum droplet diameter of 1.0  $\mu\text{m}$  was set, below which evaporation was assumed to cease. This assumption is justified because such small droplets follow the airflow and exhibit similar dynamic behavior [14]. To ensure the stability and realizability of the QMOM solver, a first-order upwind scheme was utilized.

The E-L approach was also adopted for comparison. Droplets following the measured size distribution were released at a rate of 214 droplets per second, as reported by [25]. Drag and gravity forces were included, along with the same heat and mass transfer models used in the TFM-PBE approach. An additional term was included in Equation (10) to consider the effect of the change of particle mass caused by evaporation. The same minimum droplet diameter of 1.0  $\mu\text{m}$  was adopted. The RNG  $k - \epsilon$  turbulence model was applied, and turbulent dispersion effects were considered. For droplet–wall interactions, a stick condition was specified.

Hexahedral grids, refined near walls and surfaces, were used for the simulations. Grid convergence was assessed with three grid resolutions: coarse (627,326 cells), medium (1,143,714 cells), and fine (2,280,912 cells). The results from the medium and fine grids were consistent, indicating good convergence. Consequently, the medium grid (1,143,714 cells) was selected for the simulations in this study to balance accuracy and computational cost. Details of the grid convergence study are provided in Appendix A.3.

### 3.3.2. Results and Discussion of Evaporating Droplets

Figure 14 compares the predicted velocity profiles and dimensionless concentration with experimental data, demonstrating the reliability of both the TFM-PBE and E-L approaches for tracing respiratory droplet transport indoors. Figure 14a shows a velocity peak centered at  $x = 1.75$  m along sampling line 1, caused by airflow from ventilation inlet 2, located above the sampling line (Figure 13b). Similarly, in Figure 14b, a velocity peak is observed below ventilation inlet 1 at  $y = 1.25$  m. Figure 14c presents the dimensionless droplet concentration,  $\bar{C}$ , defined as the ratio of the concentration of droplets at a given point to the average concentration at the four measurement points (P1 to P4). Fresh air reduces the concentration at points P2 and P3, located below the ventilation inlets, while higher concentrations at P1 and P4, near the mouth, indicate less effective droplet removal

in those areas. These differences highlight the ability of ventilation systems to dilute and remove respiratory droplets.

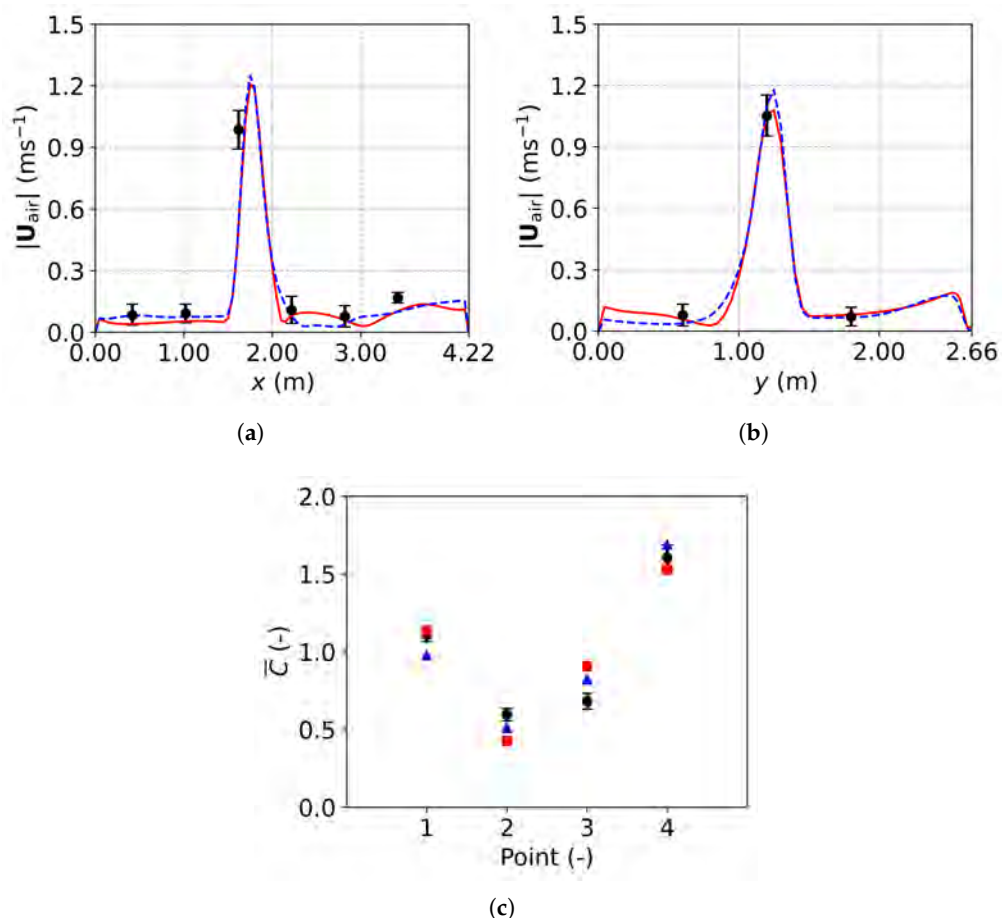


**Figure 14.** Comparison between simulation results and experimental data: (a) air velocity profile along line 1; (b) air velocity profile along line 2; (c) dimensionless concentration at the four sampling points. Black circles: experimental data [25]; red solid lines and squares: numerical results of the TFM-PBE approach; blue dashed lines and triangles: numerical results of the E-L approach.

Figures 15 and 16 compare the droplet size, velocity, and distribution obtained using the TFM-PBE and E-L approaches, respectively. Figure 15a shows the Sauter mean diameter of the droplets predicted by the TFM-PBE approach. A minimum diameter of 1  $\mu\text{m}$  was specified to represent droplet nuclei, which cease evaporating. The results indicate that droplets exceed this minimum diameter only within a small region near the mouth, confirming rapid evaporation into nuclei. This behavior aligns with our prior findings [52], where droplets of 10  $\mu\text{m}$  evaporated fully within one second, and smaller droplets evaporated even faster. This is also consistent with the experimental results of Wang et al. [25], where identical droplet size distributions were found at the four measurement points. The identical distributions represent the droplet nuclei, formed after a quick full evaporation and transported throughout the region.

The E-L approach yields a droplet size distribution similar to that of the TFM-PBE approach, as shown in Figure 16a, with most droplet diameters around 1  $\mu\text{m}$ . However, the region near the mouth containing droplets larger than 1  $\mu\text{m}$  is less pronounced in the E-L results. This discrepancy arises from the limited droplet release rate in the E-L simulations. Despite more than 40,000 droplets being introduced at a steady state—sufficient for statistically reliable results for transport analysis—the smaller sample size appears insufficient to fully capture evaporation dynamics.

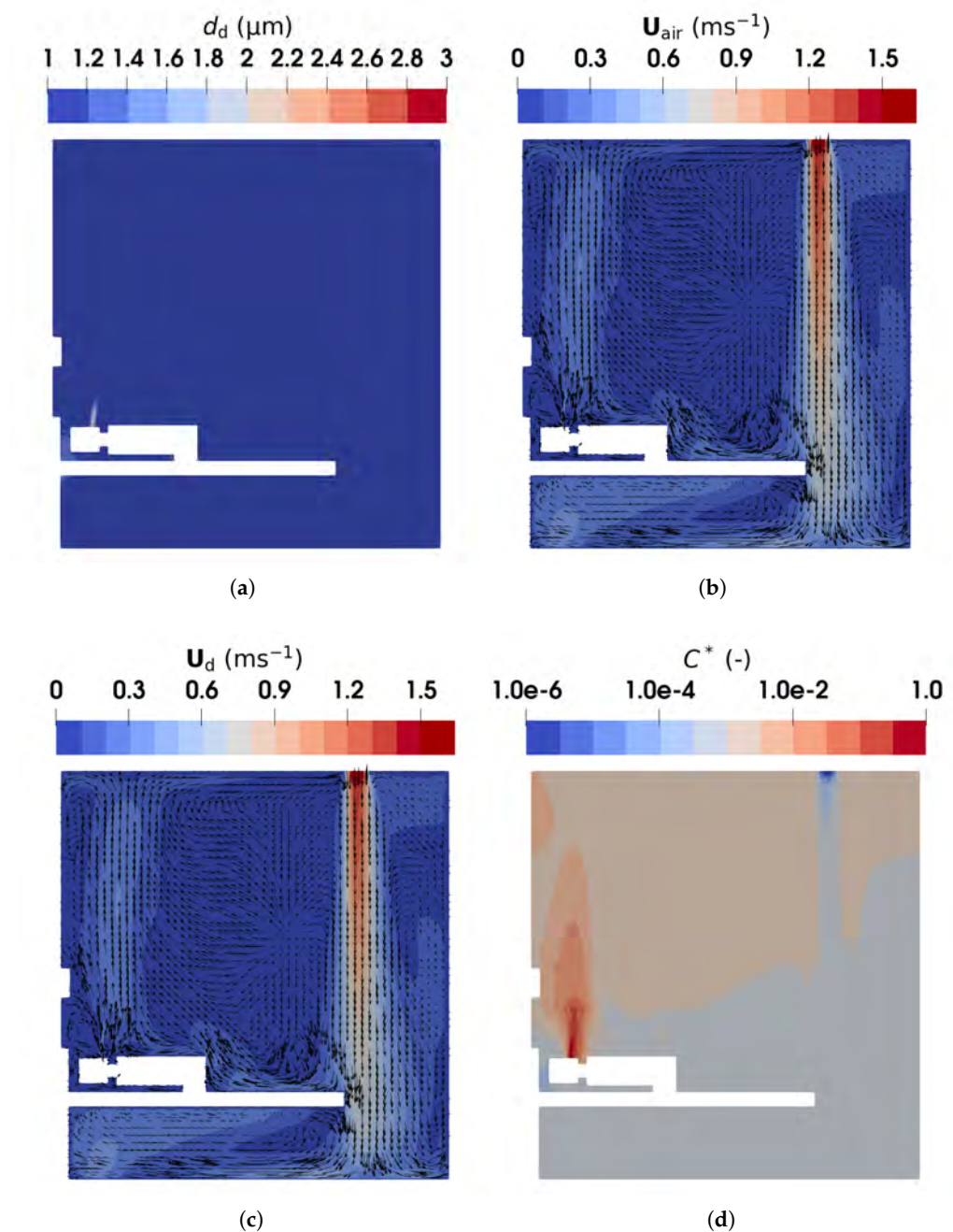


**Figure 15.** The droplet diameter, velocities, and normalized concentration contour in the vertical plane of  $x = 1.685$  m (intersecting the middle of the manikin) obtained using the TFM-PBE approach: (a) droplet diameter; (b) air velocity; (c) droplet velocity; (d) normalized concentration of droplets.

Figure 15b,c present the air and droplet velocities, showing close agreement due to the small size of the droplet nuclei. The human breath was modeled as a droplet-laden flow injected from the manikin mouth at a constant velocity of  $0.5 \text{ ms}^{-1}$ , directed upwards. This creates an upward flow with a velocity of approximately  $0.5 \text{ ms}^{-1}$  above the head of the manikin. Simultaneously, fresh air supplied from ventilation inlet 2 descends, decelerating as it moves through the ward, eventually impinging on the floor and creating near-floor airflows. Part of the descending air impinges on the bed, generating a leftward flow, which is heated by the manikin legs and trunk (see Figure S3 of the Supplementary Material for detailed temperature distribution) before merging with the upward exhaled air. Additionally, relatively high velocities are observed near the exhaust in the lower-left

corner. These airflow patterns influence droplet distribution. The E-L approach, as shown in Figure 16b, gives similar results: droplet velocities above the mouth are approximately  $0.5 \text{ ms}^{-1}$  due to the breathing and buoyant flow.

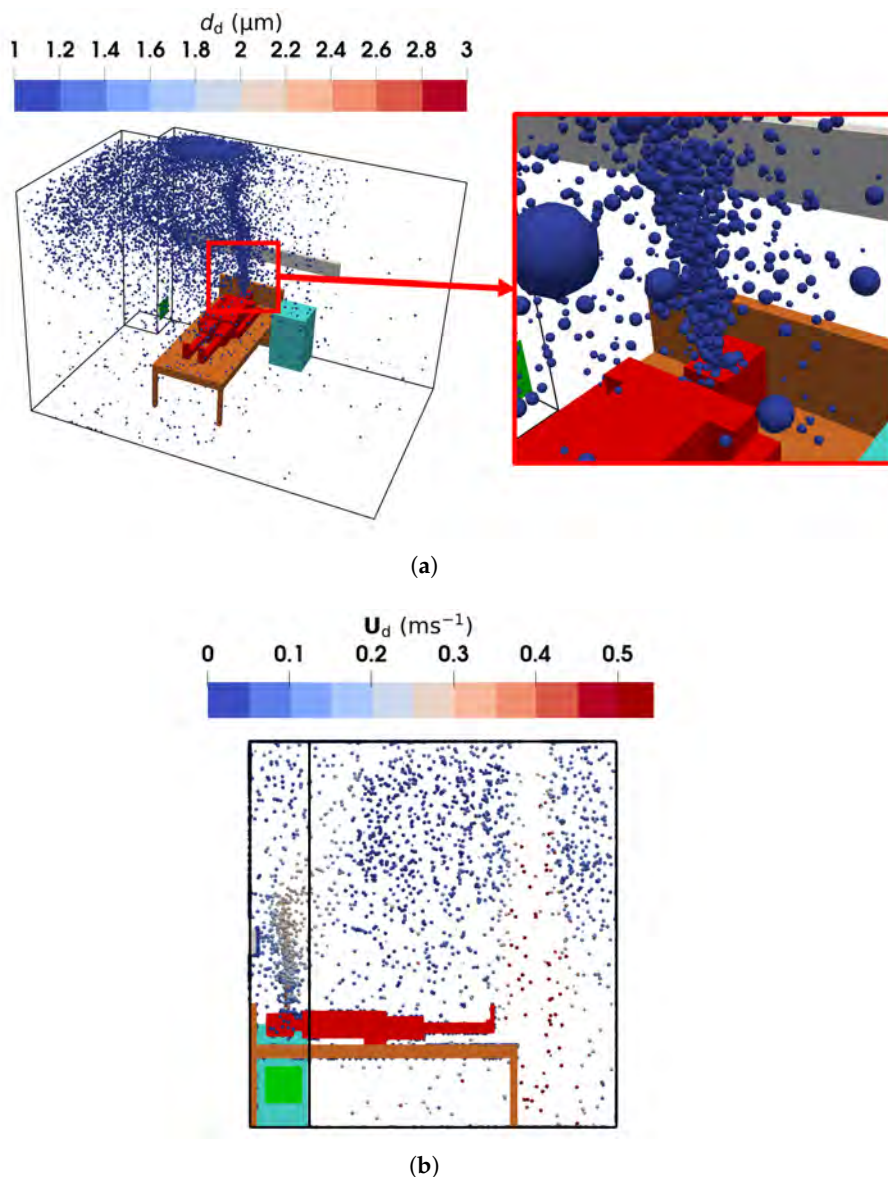


**Figure 16.** The droplet diameters and velocities obtained using the E-L approach: (a) droplet diameter and spatial distribution from the oblique view; (b) droplet velocity and spatial distribution in the sampling region from the left view (symmetric to the vertical plane of  $x = 1.685 \text{ m}$ ).

Figure 15d presents the normalized droplet number concentration with respect to the inlet value,  $C^* = M_0/M_{0,in}$ . The concentration is highest in the exhaled air near the manikin mouth and lowest in the fresh air near the ventilation inlet. Rapid evaporation transforms droplets into nuclei, which closely follow the airflow patterns. The droplets are carried by the upward airflows above the manikin head into the upper part of the ward. A similar distribution is observed in Figure 16b, where the Lagrangian droplets accumulate above the mouth and in the upper region of the ward. These results align with Wang et al. [25], who reported that droplet nuclei primarily concentrate in the upper ward area, with most depositing on the ceiling. This stratified distribution is attributed to the incomplete mixing of indoor air. The breathing airflow, with its relatively low velocity,

interacts weakly with the downward-supplied fresh air, resulting in limited mixing between the two flows.

In this case, the average computing times for every 1000 time steps using 8 CPU cores for the TFM-PBE and E-L approaches are 5.49 h and 1.27 h, respectively. Consistent with [25], a small droplet release rate of 214 droplets per second was used to simulate breathing. The limited number of tracked droplets in the E-L approach significantly reduces its computational cost. However, when a larger number of droplets is tracked, the computational advantage of the Eulerian approach becomes more pronounced.

In summary, the TFM-PBE coupled approach effectively models the transmission of evaporating droplets, yielding results comparable to the E-L approach. Small droplets rapidly evaporate into nuclei, which subsequently follow the airflow, highlighting the approach's applicability in ventilated environments.

#### 4. Conclusions

Ventilation systems play a critical role in diluting or removing virus-laden respiratory droplets in indoor environments, making their performance essential for effective infection control. This study investigated the effectiveness of different Eulerian approaches in modeling the transport of respiratory droplets under different ventilation systems (DV, SV, and MV). The analysis focused on airflow patterns, concentration fields, and the computational performance of the numerical methods. The results were compared to those of a standard Lagrangian method to test the relative performance.

The results showed that DV transports droplets to upper regions through buoyant flows, offering protection in specific areas by reducing droplet concentration. SV effectively supplies fresh air directly to the breathing zone, minimizing exposure to contaminated air. In contrast, MV achieves uniform mixing, which, while reducing overall aerosol levels, can increase infection risks by evenly distributing infectious particles. Consequently, SV and DV are preferred for infection control.

From a numerical perspective, Eulerian approaches of different complexity and computational cost are available to effectively model various droplet types: PSPM for small inert droplets that are carried passively by airflows, TFM for non-evaporating particles, and TFM-PBE for evaporating droplets. Comparisons with experimental data demonstrated that the accuracy of the Eulerian approach is comparable to that of the E-L approach. The Eulerian method is more computationally efficient for scenarios involving large numbers of particles, making it suitable for long-term simulations of respiratory activities. Meanwhile, the E-L approach excels in handling particle–wall interactions and is advantageous for studying droplet deposition in localized or short-term scenarios. These distinctions make the two approaches complementary, with the choice depending on the specific research or application needs.

Temperature significantly affects airflow in ventilated indoor environments. However, detailed temperature boundary conditions are often unavailable due to cost constraints. In future work, we will combine machine learning with experimental and numerical methods to obtain reliable and reasonable boundary conditions from limited data.

**Supplementary Materials:** The following supporting information can be downloaded at <https://www.mdpi.com/article/10.3390/fluids10070185/>. Figure S1: The temperature field of (a) DV, (b) SV, and (c) MV in the plane of  $x = 2.2$  m. Figure S2: The temperature field of the continuous air phase in the plane of  $x = 2.55$  m under (a) DV and (b) MV, and in the plane of  $z = 1.12$  m under (c) DV and (d) MV. Figure S3: The temperature field of the continuous air phase in the plane of  $x = 1.685$  m.

**Author Contributions:** Conceptualization, D.M., M.V. and A.B.; methodology, D.L., D.M., M.V. and A.B.; software, Y.F.; validation, Y.F.; formal analysis, Y.F.; investigation, Y.F.; resources, A.B.; data

curation, Y.F.; writing—original draft preparation, Y.F.; writing—review and editing, D.L., D.M., M.V. and A.B.; visualization, Y.F.; supervision, D.L., D.M., M.V. and A.B.; project administration, A.B.; funding acquisition, A.B. All authors have read and agreed to the published version of the manuscript.

**Funding:** This study was partially funded by the “Next-generation multiscale MOdelling of Dense EMulsions for enhanced multiphase flow processes (MODEM 20229WJBPS)” project by European Union–Next Generation EU within the PRIN 2022 program (D.D. 104—02/02/2022 Ministero dell’Universita e della Ricerca). This manuscript reflects only the authors’ views and opinions and the ministry cannot be considered responsible for them.

**Data Availability Statement:** Part of the data that support the findings of this study are openly available in Zenodo at <https://doi.org/10.5281/zenodo.10047638>. Part of the codes and testing cases are openly available in GitHub (accessed on 9 July 2025) at [https://github.com/mulmopro/respiratory\\_droplets](https://github.com/mulmopro/respiratory_droplets).

**Acknowledgments:** Computational resources provided by hpc@polito, which is a project of Academic Computing within the Department of Control and Computer Engineering at the Politecnico di Torino (accessed on 9 July 2025) (<http://www.hpc.polito.it>).

**Conflicts of Interest:** Author Dongyue Li was employed by the company DYFLUID Ltd. The remaining authors declare that the research was conducted in the absence of any commercial or financial relationships that could be construed as a potential conflict of interest.

## Appendix A. Grid Convergence Examination

### Appendix A.1. The Office with DV, SV and MV

For the small office equipped with DV, MV, and SV [17] discussed in Section 3.1, the grid convergence was examined using three grids having 258,232 (coarse), 553,632 (medium), and 1,222,930 (fine) cube cells, respectively. The setups of MV were adopted. The computing time increased by a factor of about 1.5 from a coarse to a medium to a fine grid. The results are shown in Figure A1. It can be seen that the results of the medium grid and the fine grid were very close. Furthermore, the surface average mass fraction of CO<sub>2</sub>,  $Y_{CO_2}$ , at the outlet for the coarse, medium, and fine grids were  $1.6203 \times 10^{-3}$ ,  $1.5821 \times 10^{-3}$ , and  $1.5803 \times 10^{-3}$ , respectively. The difference in medium and fine grids was small. Considering the computational costs and accuracy, the medium grid with 553,632 cells (Figure A4a) was adopted for the simulations in this study.

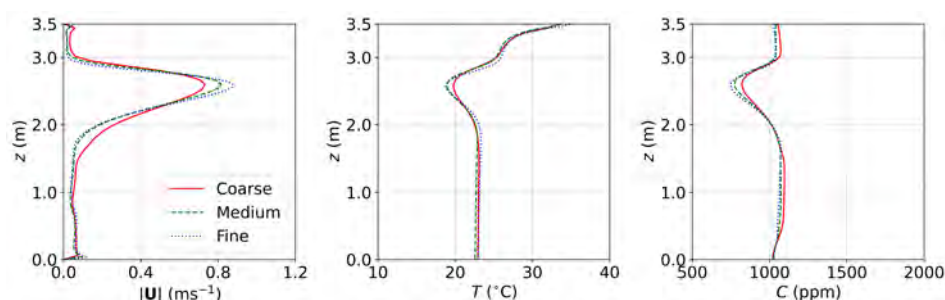


**Figure A1.** The results of grid convergence examination for the small office with DV, SV, and MV. Red solid lines: coarse grid; green dashed lines: medium grid; blue dash-dotted lines: fine grid.

### Appendix A.2. The Office with DV and MV

For the office equipped with DV and MV [22] of Section 3.2, the grid convergence was examined using three grids having 964,947 (coarse), 1,965,986 (medium), and 4,571,857 (fine) cube cells, respectively. The setups of MV were specified. The computing time increased by a factor of about 1.2 with each level of grid refinement. The results are shown in Figure A2. It can be seen that the results of the medium grid and the fine grid were very close. In addition, the surface average particle concentration at the outlet for the three sets of grids were

$4.92 \times 10^9 \text{ m}^{-3}$ ,  $5.17 \times 10^9 \text{ m}^{-3}$ , and  $5.16 \times 10^9 \text{ m}^{-3}$ , respectively. The difference between the medium and fine grids was small. Considering the computational costs and accuracy, the medium grid with 1,965,986 cells (Figure A4b) was adopted for the simulations in this study.

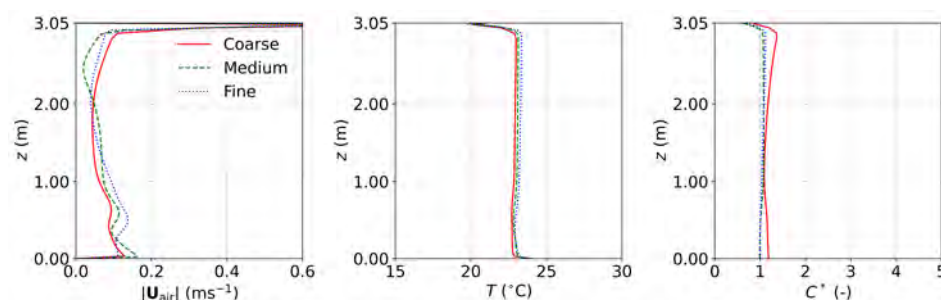


**Figure A2.** The results of grid convergence examination for the office with DV and MV. Red solid lines: coarse grid; green dashed lines: medium grid; blue dash-dotted lines: fine grid.

*Appendix A.3. The Negative-Pressure Isolation Ward*

For the negative pressure isolation ward equipped with MV [25] (Section 3.3), the grid convergence was examined using three grids with 627,326 (coarse), 1,143,714 (medium), and 2,280,912 (fine) cube cells, respectively. The computing time for the three grids increased by a factor of about 1.5 with each level of grid refinement. The velocity profiles predicted using the three grids are shown in Figure A3. It can be seen that the results of the medium grid and the fine grid were very close. In addition, the mass flow rate at the outlet of the coarse, medium, and fine grids were  $0.1170 \text{ kg s}^{-1}$ ,  $0.1192 \text{ kg s}^{-1}$ , and  $0.1196 \text{ kg s}^{-1}$ , respectively. The difference between the medium and the fine grids is small. Considering the computational costs and accuracy, the medium grid with 1,143,714 cells (Figure A4c) was adopted for the simulations in this study.

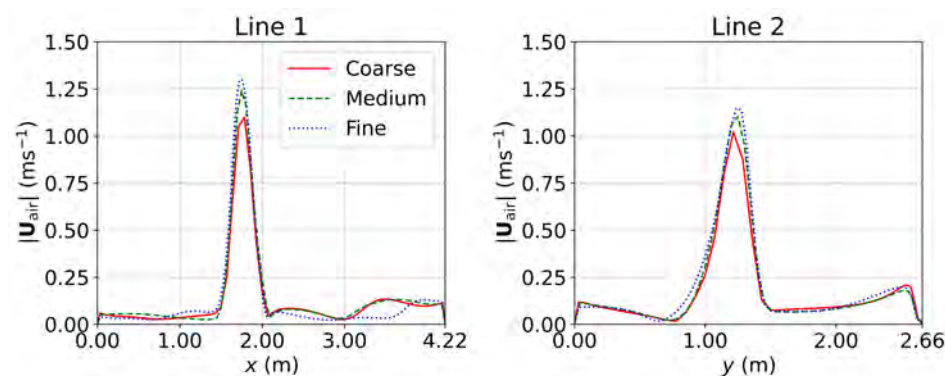


**Figure A3.** The results of grid convergence examination for the negative-pressure isolation ward with MV. Red solid lines: coarse grid; green dashed lines: medium grid; blue dash-dotted lines: fine grid.

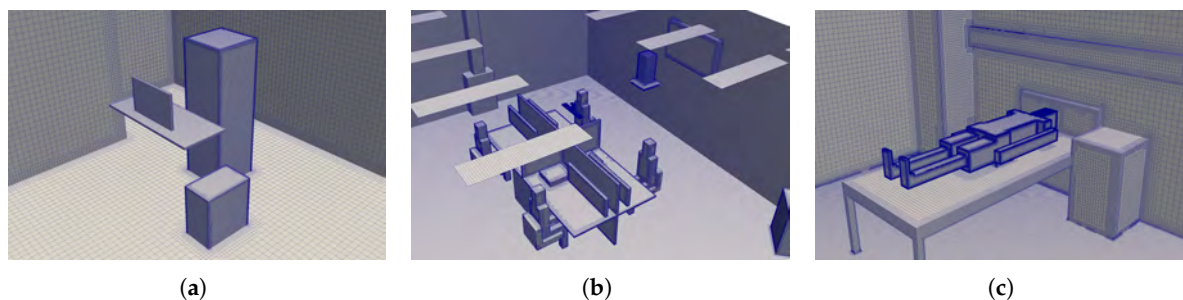


**Figure A4.** The oblique view of the medium grids of: (a) the office with DV, MV, and SV [17]; (b) the office with DV and MV [22]; (c) the ward with MV [25].

## Appendix B. Boundary Conditions

Tables A1 and A2 present the boundary conditions for the small office with DV, SV, and MV [17]. Six cases are investigated in this study: three ventilation systems each having two different CO<sub>2</sub> source locations.

Tables A3 and A4 present the boundary conditions for the office with DV and MV [22].

Table A5 presents the boundary conditions for the isolation ward with MV [25].

**Table A1.** The boundary conditions for the office equipped with DV, SV, and MV.

Ventilations	Variables	Inlet	Exhaust	Walls and Surfaces				
				Manikin	Floor	Fluorescents	System Unit	Others
DV	U	0.16 ms <sup>-1</sup> (33.2%) <sup>1</sup> , fixedValue	free outgoing, zeroGradient			no-slip, noSlip		
	T	12.6 °C, fixedValue	free outgoing, zeroGradient	100 W, eWHFT <sup>2</sup>	23.0 °C, fixedValue	72 W, eWHFT	180 W, eWHFT	adiabatic, zeroGradient
	<i>p<sub>rgh</sub></i>	incoming, fixedFluxPressure	101,325 Pa, fixedValue			no outflow, fixedFluxPressure		
	<i>k</i>	9.6 × 10 <sup>-5</sup> m <sup>2</sup> s <sup>-2</sup> , fixedValue	free outgoing, zeroGradient			wall function, kqRWallFunction		
	<i>ε</i>	7.0 × 10 <sup>-6</sup> m <sup>2</sup> s <sup>-3</sup> , fixedValue	free outgoing, zeroGradient			wall function, epsilonWallFunction		
	<i>α<sub>t</sub></i>	calculated, calculated	free outgoing, zeroGradient			wall function, alphasWallFunction		
	<i>v<sub>t</sub></i>	calculated, calculated	free outgoing, zeroGradient			wall function, nutkWallFunction		
SV	U	2.16 ms <sup>-1</sup> (82.7%), fixedValue	free outgoing, zeroGradient			no-slip, noSlip		
	T	15.5 °C, fixedValue	free outgoing, zeroGradient	100 W, eWHFT	27.1 °C, fixedValue	72 W, eWHFT	180 W, eWHFT	adiabatic, zeroGradient
	<i>p<sub>rgh</sub></i>	incoming, fixedFluxPressure	101,325 Pa, fixedValue			no outflow, fixedFluxPressure		
	<i>k</i>	1.2 × 10 <sup>-2</sup> m <sup>2</sup> s <sup>-2</sup> , fixedValue	free outgoing, zeroGradient			wall function, kqRWallFunction		
	<i>ε</i>	4.6 × 10 <sup>-2</sup> m <sup>2</sup> s <sup>-3</sup> , fixedValue	free outgoing, zeroGradient			wall function, epsilonWallFunction		
	<i>α<sub>t</sub></i>	calculated, calculated	free outgoing, zeroGradient			wall function, alphasWallFunction		
	<i>v<sub>t</sub></i>	calculated, calculated	free outgoing, zeroGradient			wall function, nutkWallFunction		
MV	U	2.16 ms <sup>-1</sup> (79.7%), fixedValue	free outgoing, zeroGradient			no-slip, noSlip		
	T	11.3 °C, fixedValue	free outgoing, zeroGradient	100 W, eWHFT	24.0 °C, fixedValue	72 W, eWHFT	180 W, eWHFT	adiabatic, zeroGradient
	<i>p<sub>rgh</sub></i>	incoming, fixedFluxPressure	101,325 Pa, fixedValue			no outflow, fixedFluxPressure		
	<i>k</i>	1.2 × 10 <sup>-2</sup> m <sup>2</sup> s <sup>-2</sup> , fixedValue	free outgoing, zeroGradient			wall function, kqRWallFunction		
	<i>ε</i>	4.6 × 10 <sup>-2</sup> m <sup>2</sup> s <sup>-3</sup> , fixedValue	free outgoing, zeroGradient			wall function, epsilonWallFunction		
	<i>α<sub>t</sub></i>	calculated, calculated	free outgoing, zeroGradient			wall function, alphasWallFunction		
	<i>v<sub>t</sub></i>	calculated, calculated	free outgoing, zeroGradient			wall function, nutkWallFunction		

<sup>1</sup> The method of Zhang et al. [60] is adopted for the inlet boundary condition, where the measured supply air velocity is specified as 0.16 ms<sup>-1</sup> for 33.2% of the inlet area to match the supply airflow rate. <sup>2</sup> eWHFT is the abbreviation of externalWallHeatFluxTemperature, which provides a fixed power rate boundary condition.

**Table A2.** The inlet boundary conditions and source intensities of water vapor and CO<sub>2</sub>.

Source Locations	Cases	Y <sub>H<sub>2</sub>O</sub> at Inlet	Y <sub>CO<sub>2</sub></sub> at Inlet	S <sub>CO<sub>2</sub></sub> Source Intensity
armpit, (2.40 m, 0.95 m, 1.00 m)	DV-A1	1.04 × 10 <sup>-2</sup> <sup>1</sup>	5.87 × 10 <sup>-4</sup> <sup>2</sup>	3.55 × 10 <sup>-5</sup> kgs <sup>-1</sup> <sup>2</sup>
	SV-A1	1.01 × 10 <sup>-2</sup>	4.92 × 10 <sup>-4</sup>	4.39 × 10 <sup>-5</sup> kgs <sup>-1</sup>
	MV-A1	1.25 × 10 <sup>-2</sup>	6.59 × 10 <sup>-4</sup>	3.33 × 10 <sup>-5</sup> kgs <sup>-1</sup>
floor, (2.35 m, 2.20 m, 0.00 m)	DV-F1	1.04 × 10 <sup>-2</sup>	6.37 × 10 <sup>-4</sup>	3.64 × 10 <sup>-5</sup> kgs <sup>-1</sup>
	SV-F1	1.01 × 10 <sup>-2</sup>	4.73 × 10 <sup>-4</sup>	4.46 × 10 <sup>-5</sup> kgs <sup>-1</sup>
	MV-F1	1.25 × 10 <sup>-2</sup>	6.04 × 10 <sup>-4</sup>	3.66 × 10 <sup>-5</sup> kgs <sup>-1</sup>

<sup>1</sup> This is calculated by the room air relative humidity provided in Tian et al. [17]. <sup>2</sup> This is calculated by the contaminant removal effectiveness provided in Tian et al. [17]. The source term is specified by fvOptions of OpenFOAM.

**Table A3.** The boundary conditions for the office equipped with DV and MV.

Ventilations	Variables	Ventilation Inlet	Emitter Inlet	Exhaust	Walls and Surfaces <sup>1</sup>
DV	$\alpha_c$	1.0, <i>fixedValue</i>	0.999999, <i>fixedValue</i>	free outgoing, <i>zeroGradient</i>	no deposition, <i>zeroGradient</i>
	$\alpha_d$	0.0, <i>fixedValue</i>	0.000001, <i>fixedValue</i>	free outgoing, <i>zeroGradient</i>	no deposition, <i>zeroGradient</i>
	$U_c$ and $U_d$ <sup>2</sup>	1.02 ms <sup>-1</sup> (22.1%), <i>fixedValue</i>	1.58 ms <sup>-1</sup> , <i>fixedValue</i>	free outgoing, <i>zeroGradient</i>	no-slip, <i>noSlip</i>
	$p_{rgh}$	incoming, <i>fixedFluxPressure</i>	incoming, <i>fixedFluxPressure</i>	101,325 Pa, <i>fixedValue</i>	no outflow, <i>fixedFluxPressure</i>
	$k_c$	$3.9 \times 10^{-3}$ m <sup>2</sup> s <sup>-2</sup> , <i>fixedValue</i>	$3.7 \times 10^{-2}$ m <sup>2</sup> s <sup>-2</sup> , <i>fixedValue</i>	free outgoing, <i>zeroGradient</i>	wall function, <i>kqRWallFunction</i>
	$\epsilon_c$	$1.4 \times 10^{-3}$ m <sup>2</sup> s <sup>-3</sup> , <i>fixedValue</i>	$1.1 \times 10^{-1}$ m <sup>2</sup> s <sup>-3</sup> , <i>fixedValue</i>	free outgoing, <i>zeroGradient</i>	wall function, <i>epsilonWallFunction</i>
	$\alpha_{t,c}$	calculated, <i>calculated</i>	calculated, <i>calculated</i>	free outgoing, <i>zeroGradient</i>	wall function, <i>alphatWallFunction</i>
$\nu_{t,c}$	calculated, <i>calculated</i>	calculated, <i>calculated</i>	free outgoing, <i>zeroGradient</i>	wall function, <i>nutkWallFunction</i>	
MV	$\alpha_c$	1.0, <i>fixedValue</i>	0.999999, <i>fixedValue</i>	free outgoing, <i>zeroGradient</i>	no deposition, <i>zeroGradient</i>
	$\alpha_d$	0.0, <i>fixedValue</i>	0.000001, <i>fixedValue</i>	free outgoing, <i>zeroGradient</i>	no deposition, <i>zeroGradient</i>
	$U_c$ and $U_d$	2.74 ms <sup>-1</sup> , <sup>3</sup> <i>fixedValue</i>	1.58 ms <sup>-1</sup> , <i>fixedValue</i>	free outgoing, <i>zeroGradient</i>	no-slip, <i>noSlip</i>
	$p_{rgh}$	incoming, <i>fixedFluxPressure</i>	incoming, <i>fixedFluxPressure</i>	101,325 Pa, <i>fixedValue</i>	no outflow, <i>fixedFluxPressure</i>
	$k_c$	0.25 m <sup>2</sup> s <sup>-2</sup> , <i>fixedValue</i>	$3.7 \times 10^{-2}$ m <sup>2</sup> s <sup>-2</sup> , <i>fixedValue</i>	free outgoing, <i>zeroGradient</i>	wall function, <i>kqRWallFunction</i>
	$\epsilon_c$	2.1 m <sup>2</sup> s <sup>-3</sup> , <i>fixedValue</i>	$1.1 \times 10^{-1}$ m <sup>2</sup> s <sup>-3</sup> , <i>fixedValue</i>	free outgoing, <i>zeroGradient</i>	wall function, <i>epsilonWallFunction</i>
	$\alpha_{t,c}$	calculated, <i>calculated</i>	calculated, <i>calculated</i>	free outgoing, <i>zeroGradient</i>	wall function, <i>alphatWallFunction</i>
$\nu_{t,c}$	calculated, <i>calculated</i>	calculated, <i>calculated</i>	free outgoing, <i>zeroGradient</i>	wall function, <i>nutkWallFunction</i>	

<sup>1</sup> This includes all walls and surfaces, such as the surfaces of manikins, computers, and TV. <sup>2</sup> The continuous phase and dispersed phase have the same velocity boundary conditions. For the ventilation inlet, the method of Zhang et al. [60] is adopted for the DV, where a velocity of 1.02 ms<sup>-1</sup> is specified for 22.1% of the inlet area as in the experiment. The emitter inlet velocity is specified as in the experiment. <sup>3</sup> The MV inlet velocity is calculated for the airflow rate of 4 ACH based on the simplified geometry in this study.

**Table A4.** The temperature boundary conditions for the office equipped with DV and MV.

Boundaries	DV	MV
Ventilation inlet	16.7 °C, <i>fixedValue</i>	12.9/12.5 °C <sup>1</sup> , <i>fixedValue</i>
Emitter inlet <sup>2</sup>	23.4 °C, <i>fixedValue</i>	22.7 °C, <i>fixedValue</i>
Fluorescents <sup>3</sup>	46.85 °C, <i>fixedValue</i>	46.85 °C, <i>fixedValue</i>
Manikin <sup>4</sup>	31.0 °C, <i>fixedValue</i>	31.0 °C, <i>fixedValue</i>
TV <sup>4</sup>	30.2 °C, <i>fixedValue</i>	30.2 °C, <i>fixedValue</i>
Computer <sup>4</sup>	33.0 °C, <i>fixedValue</i>	33.0 °C, <i>fixedValue</i>
Monitor <sup>4</sup>	29.6 °C, <i>fixedValue</i>	29.6 °C, <i>fixedValue</i>
Floor ( $z = 0$ m) <sup>4</sup>	24.0 °C, <i>fixedValue</i>	24.0 °C, <i>fixedValue</i>
Left-hand wall ( $y = 5.8$ m) <sup>4</sup>	25.0 °C, <i>fixedValue</i>	25.0 °C, <i>fixedValue</i>
Right-hand wall ( $y = 0$ m) <sup>4</sup>	25.2 °C, <i>fixedValue</i>	25.2 °C, <i>fixedValue</i>
Front wall ( $x = 7.0$ m) <sup>4</sup>	25.0 °C, <i>fixedValue</i>	25.0 °C, <i>fixedValue</i>

Table A4. Cont.

Boundaries	DV	MV
Back wall ( $x = 0\text{ m}$ ) <sup>4</sup>	25.6 °C, <i>fixedValue</i>	25.6 °C, <i>fixedValue</i>
Back wall ( $x = 0\text{ m}$ ) <sup>4</sup>	25.6 °C, <i>fixedValue</i>	25.6 °C, <i>fixedValue</i>
Ceiling ( $z = 3.05\text{ m}$ ) <sup>5</sup>	21.0 °C, <i>fixedValue</i>	21.0 °C, <i>fixedValue</i>
Other surfaces <sup>6</sup>	adiabatic, <i>zeroGradient</i>	adiabatic, <i>zeroGradient</i>

<sup>1</sup> There are two MV inlets; the left one is 12.9 ms<sup>-1</sup> and the right one is 12.5 ms<sup>-1</sup>. <sup>2</sup> The temperature of the emitted particles was not provided, and the measured room temperature was specified for the particles. <sup>3</sup> A fixed temperature was specified for all fluorescents, which provided a power rate close to that given in the experiment [22]. <sup>4</sup> The measured temperature was only given for MV in the paper [22]. The same value was used for the DV in this study. <sup>5</sup> The paper [22] did not provide the ceiling temperature, so a temperature that provided good agreement was adopted in this study. <sup>6</sup> The paper [22] did not provide the temperatures of other surfaces, so an adiabatic boundary condition was adopted.

Table A5. The boundary conditions for the isolation ward with MV.

Variables	MV Inlet	Mouth	Door Gap 1/2	Exhaust	Manikin	Walls and Surfaces
$\alpha_c$	1.0, <i>fixedValue</i>	0.999999, <i>fixedValue</i>	1.0/1.0, <i>fixedValue</i>	free outgoing, <i>zeroGradient</i>	no deposition, <i>zeroGradient</i>	no deposition, <i>zeroGradient</i>
$\alpha_d$	0.0, <i>fixedValue</i>	0.000001, <i>fixedValue</i>	0.0/0.0, <i>fixedValue</i>	free outgoing, <i>zeroGradient</i>	no deposition, <i>zeroGradient</i>	no deposition, <i>zeroGradient</i>
$U_c$ and $U_d$	1.5 ms <sup>-1</sup> , <i>fixedValue</i>	0.5 ms <sup>-1</sup> , <i>fixedValue</i>	2.0/−2.3 ms <sup>-1</sup> , <i>fixedValue</i>	free outgoing, <i>zeroGradient</i>	no-slip, <i>noSlip</i>	no-slip, <i>noSlip</i>
$T_c$ and $T_d$	299.1 K, <i>fixedValue</i>	309.1 K, <i>fixedValue</i>	299.1/299.1 K, <i>fixedValue</i>	free outgoing, <i>zeroGradient</i>	307.1 K, <i>fixedValue</i>	adiabatic, <i>zeroGradient</i>
$P_{rgh}$	incoming, <i>fixedFluxPressure</i>	incoming, <i>fixedFluxPressure</i>	incoming, <i>fixedFluxPressure</i>	101,325 Pa, <i>fixedValue</i>	no outflow, <i>fixedFluxPressure</i>	no outflow, <i>fixedFluxPressure</i>
$k_c$	$9.4 \times 10^{-3}\text{ m}^2\text{s}^{-2}$ , <i>fixedValue</i>	$9.4 \times 10^{-4}\text{ m}^2\text{s}^{-2}$ , <i>fixedValue</i>	0.015/0.020 m <sup>2</sup> s <sup>-2</sup> , <i>fixedValue</i>	free outgoing, <i>zeroGradient</i>	wall function, <i>kqRWallFunction</i>	wall function, <i>kqRWallFunction</i>
$\epsilon_c$	$1.2 \times 10^{-2}\text{ m}^2\text{s}^{-3}$ , <i>fixedValue</i>	$3.4 \times 10^{-3}\text{ m}^2\text{s}^{-3}$ , <i>fixedValue</i>	0.11/0.17 m <sup>2</sup> s <sup>-3</sup> , <i>fixedValue</i>	free outgoing, <i>zeroGradient</i>	wall function, <i>epsilonWallFunction</i>	wall function, <i>epsilonWallFunction</i>
$\alpha_{t,c}$	calculated, <i>calculated</i>	calculated, <i>calculated</i>	calculated, <i>calculated</i>	free outgoing, <i>zeroGradient</i>	wall function, <i>alphanWallFunction</i>	wall function, <i>alphanWallFunction</i>
$\nu_{t,c}$	calculated, <i>calculated</i>	calculated, <i>calculated</i>	calculated, <i>calculated</i>	free outgoing, <i>zeroGradient</i>	wall function, <i>nutkWallFunction</i>	wall function, <i>nutkWallFunction</i>
$M_i$	0.0, <i>fixedValue</i>	Table 3, <i>fixedValue</i>	0.0/0.0, <i>fixedValue</i>	free outgoing, <i>zeroGradient</i>	no deposition, <i>zeroGradient</i>	no deposition, <i>zeroGradient</i>
$Y_{H_2O}$	0.012, <i>fixedValue</i>	0.033, <i>fixedValue</i>	0.012/0.012, <i>fixedValue</i>	free outgoing, <i>zeroGradient</i>	no outflow, <i>zeroGradient</i>	no outflow, <i>zeroGradient</i>

<sup>1</sup> Air flowed into the ward at door gap 1 and flowed out of the ward at door gap 2.

References

1. WHO. *Transmission of SARS-CoV-2: Implications for Infection Prevention Precautions*; Technical Report; World Health Organization: Geneva, Switzerland, 2020.
2. Klepeis, N.E.; Nelson, W.C.; Ott, W.R.; Robinson, J.P.; Tsang, A.M.; Switzer, P.; Behar, J.V.; Hern, S.C.; Engelmann, W.H. The National Human Activity Pattern Survey (NHAPS): A Resource for Assessing Exposure to Environmental Pollutants. *J. Expo. Sci. Environ. Epidemiol.* **2001**, *11*, 231–252. [CrossRef]
3. Chao, C.; Wan, M.; Morawska, L.; Johnson, G.; Ristovski, Z.; Hargreaves, M.; Mengersen, K.; Corbett, S.; Li, Y.; Xie, X.; et al. Characterization of Expiration Air Jets and Droplet Size Distributions Immediately at the Mouth Opening. *J. Aerosol Sci.* **2009**, *40*, 122–133. [CrossRef] [PubMed]
4. Balachandar, S.; Zaleski, S.; Soldati, A.; Ahmadi, G.; Bourouiba, L. Host-to-Host Airborne Transmission as a Multiphase Flow Problem for Science-Based Social Distance Guidelines. *Int. J. Multiph. Flow* **2020**, *132*, 103439. [CrossRef]
5. Liu, J.; Duan, Y. Saliva: A Potential Media for Disease Diagnostics and Monitoring. *Oral Oncol.* **2012**, *48*, 569–577. [CrossRef]
6. Hatif, I.H.; Mohamed Kamar, H.; Kamsah, N.; Wong, K.Y.; Tan, H. Influence of Office Furniture on Exposure Risk to Respiratory Infection under Mixing and Displacement Air Distribution Systems. *Build. Environ.* **2023**, *239*, 110292. [CrossRef]
7. Li, X.; Shang, Y.; Yan, Y.; Yang, L.; Tu, J. Modelling of Evaporation of Cough Droplets in Inhomogeneous Humidity Fields Using the Multi-Component Eulerian-Lagrangian Approach. *Build. Environ.* **2018**, *128*, 68–76. [CrossRef]
8. Tang, J.; Noakes, C.; Nielsen, P.; Eames, I.; Nicolle, A.; Li, Y.; Settles, G. Observing and Quantifying Airflows in the Infection Control of Aerosol- and Airborne-Transmitted Diseases: An Overview of Approaches. *J. Hosp. Infect.* **2011**, *77*, 213–222. [CrossRef]
9. Cao, G.; Sirén, K.; Kilpeläinen, S. Modelling and Experimental Study of Performance of the Protected Occupied Zone Ventilation. *Energy Build.* **2014**, *68*, 515–531. [CrossRef]

10. Olmedo, I.; Nielsen, P.V.; Ruiz de Adana, M.; Jensen, R.L.; Grzelecki, P. Distribution of Exhaled Contaminants and Personal Exposure in a Room Using Three Different Air Distribution Strategies: Distribution of Exhaled Contaminants. *Indoor Air* **2012**, *22*, 64–76. [[CrossRef](#)]
11. Yang, J.; Sekhar, S.C.; Cheong, K.W.D.; Raphael, B. Performance Evaluation of a Novel Personalized Ventilation-Personalized Exhaust System for Airborne Infection Control. *Indoor Air* **2015**, *25*, 176–187. [[CrossRef](#)]
12. Tung, Y.C.; Shih, Y.C.; Hu, S.C.; Chang, Y.L. Experimental Performance Investigation of Ventilation Schemes in a Private Bathroom. *Build. Environ.* **2010**, *45*, 243–251. [[CrossRef](#)]
13. Lu, Y.; Oladokun, M.; Lin, Z. Reducing the Exposure Risk in Hospital Wards by Applying Stratum Ventilation System. *Build. Environ.* **2020**, *183*, 107204. [[CrossRef](#)]
14. Ai, Z.; Mak, C.M.; Gao, N.; Niu, J. Tracer Gas Is a Suitable Surrogate of Exhaled Droplet Nuclei for Studying Airborne Transmission in the Built Environment. *Build. Simul.* **2020**, *13*, 489–496. [[CrossRef](#)] [[PubMed](#)]
15. Bivolarova, M.; Ondráček, J.; Melikov, A.; Ždímal, V. A Comparison between Tracer Gas and Aerosol Particles Distribution Indoors: The Impact of Ventilation Rate, Interaction of Airflows, and Presence of Objects. *Indoor Air* **2017**, *27*, 1201–1212. [[CrossRef](#)] [[PubMed](#)]
16. Rivas, E.; Santiago, J.L.; Martín, F.; Martilli, A. Impact of Natural Ventilation on Exposure to SARS-CoV-2 in Indoor/Semi-Indoor Terraces Using CO<sub>2</sub> Concentrations as a Proxy. *J. Build. Eng.* **2022**, *46*, 103725. [[CrossRef](#)]
17. Tian, X.; Li, B.; Ma, Y.; Liu, D.; Li, Y.; Cheng, Y. Experimental Study of Local Thermal Comfort and Ventilation Performance for Mixing, Displacement and Stratum Ventilation in an Office. *Sustain. Cities Soc.* **2019**, *50*, 101630. [[CrossRef](#)]
18. Ameen, A.; Cehlin, M.; Larsson, U.; Karimipannah, T. Experimental Investigation of the Ventilation Performance of Different Air Distribution Systems in an Office Environment—Cooling Mode. *Energies* **2019**, *12*, 1354. [[CrossRef](#)]
19. Kong, X.; Chang, Y.; Fan, M.; Li, H. Analysis on the Thermal Performance of Low-Temperature Radiant Floor Coupled with Intermittent Stratum Ventilation (LTR-ISV) for Space Heating. *Energy Build.* **2023**, *278*, 112623. [[CrossRef](#)]
20. Kong, X.; Wang, Z.; Fan, M.; Li, H. Analysis on the Energy Efficiency, Thermal Performance and Infection Intervention Characteristics of Interactive Cascade Ventilation (ICV). *J. Build. Eng.* **2023**, *68*, 106045. [[CrossRef](#)]
21. Zhou, Y.; Ji, S. Experimental and Numerical Study on the Transport of Droplet Aerosols Generated by Occupants in a Fever Clinic. *Build. Environ.* **2021**, *187*, 107402. [[CrossRef](#)]
22. Liu, S.; Koupriyanov, M.; Paskaruk, D.; Fediuk, G.; Chen, Q. Investigation of Airborne Particle Exposure in an Office with Mixing and Displacement Ventilation. *Sustain. Cities Soc.* **2022**, *79*, 103718. [[CrossRef](#)] [[PubMed](#)]
23. Zhuang, X.; Xu, Y.; Zhang, L.; Li, X.; Lu, J. Experiment and Numerical Investigation of Inhalable Particles and Indoor Environment with Ventilation System. *Energy Build.* **2022**, *271*, 112309. [[CrossRef](#)] [[PubMed](#)]
24. Xu, J.; Guo, H.; Zhang, Y.; Lyu, X. Effectiveness of Personalized Air Curtain in Reducing Exposure to Airborne Cough Droplets. *Build. Environ.* **2022**, *208*, 108586. [[CrossRef](#)]
25. Wang, Y.; Liu, Z.; Liu, H.; Wu, M.; He, J.; Cao, G. Droplet Aerosols Transportation and Deposition for Three Respiratory Behaviors in a Typical Negative Pressure Isolation Ward. *Build. Environ.* **2022**, *219*, 109247. [[CrossRef](#)]
26. Na, H.; Kim, H.; Kim, T. Dispersion of Droplets Due to the Use of Air Purifiers during Summer: Focus on the Spread of COVID-19. *Build. Environ.* **2023**, *234*, 110136. [[CrossRef](#)]
27. Zhong, K.; Yang, X.; Kang, Y. Effects of Ventilation Strategies and Source Locations on Indoor Particle Deposition. *Build. Environ.* **2010**, *45*, 655–662. [[CrossRef](#)]
28. Makhoul, A.; Ghali, K.; Ghaddar, N.; Chakroun, W. Investigation of Particle Transport in Offices Equipped with Ceiling-Mounted Personalized Ventilators. *Build. Environ.* **2013**, *63*, 97–107. [[CrossRef](#)]
29. Li, T.; Essah, E.A.; Wu, Y.; Cheng, Y.; Liao, C. Numerical Comparison of Exhaled Particle Dispersion under Different Air Distributions for Winter Heating. *Sustain. Cities Soc.* **2023**, *89*, 104342. [[CrossRef](#)]
30. Huang, X.; Saha, S.C.; Saha, G.; Francis, I.; Luo, Z. Transport and Deposition of Microplastics and Nanoplastics in the Human Respiratory Tract. *Environ. Adv.* **2024**, *16*, 100525. [[CrossRef](#)]
31. Talaat, M.; Si, X.; Xi, J. Evaporation Dynamics and Dosimetry Methods in Numerically Assessing MDI Performance in Pulmonary Drug Delivery. *Fluids* **2024**, *9*, 286. [[CrossRef](#)]
32. Huang, X.; Yin, Y.; Saha, G.; Francis, I.; Saha, S.C. A Comprehensive Numerical Study on the Transport and Deposition of Nasal Sprayed Pharmaceutical Aerosols in a Nasal-To-Lung Respiratory Tract Model. *Part. Part. Syst. Charact.* **2025**, *42*, 2400004. [[CrossRef](#)]
33. Wang, L.; Dai, X.; Wei, J.; Ai, Z.; Fan, Y.; Tang, L.; Jin, T.; Ge, J. Numerical Comparison of the Efficiency of Mixing Ventilation and Impinging Jet Ventilation for Exhaled Particle Removal in a Model Intensive Care Unit. *Build. Environ.* **2021**, *200*, 107955. [[CrossRef](#)]
34. Ren, J.; Wang, Y.; Liu, Q.; Liu, Y. Numerical Study of Three Ventilation Strategies in a Prefabricated COVID-19 Inpatient Ward. *Build. Environ.* **2021**, *188*, 107467. [[CrossRef](#)]

35. Liu, S.; Deng, Z. Transmission and Infection Risk of COVID-19 When People Coughing in an Elevator. *Build. Environ.* **2023**, *238*, 110343. [[CrossRef](#)] [[PubMed](#)]
36. Borro, L.; Mazzei, L.; Raponi, M.; Piscitelli, P.; Miani, A.; Secinaro, A. The Role of Air Conditioning in the Diffusion of Sars-CoV-2 in Indoor Environments: A First Computational Fluid Dynamic Model, Based on Investigations Performed at the Vatican State Children's Hospital. *Environ. Res.* **2021**, *193*, 110343. [[CrossRef](#)] [[PubMed](#)]
37. Li, X.; Feng, B. Transmission of Droplet Aerosols in an Elevator Cabin: Effect of the Ventilation Mode. *Build. Environ.* **2023**, *236*, 110261. [[CrossRef](#)]
38. Lu, Y.; Lin, Z. Coughed Droplet Dispersion Pattern in Hospital Ward under Stratum Ventilation. *Build. Environ.* **2022**, *208*, 108602. [[CrossRef](#)]
39. Zhang, Y.; Feng, G.; Bi, Y.; Cai, Y.; Zhang, Z.; Cao, G. Distribution of Droplet Aerosols Generated by Mouth Coughing and Nose Breathing in an Air-Conditioned Room. *Sustain. Cities Soc.* **2019**, *51*, 101721. [[CrossRef](#)]
40. Bensaid, S.; Marchisio, D.; Fino, D.; Saracco, G.; Specchia, V. Modelling of Diesel Particulate Filtration in Wall-Flow Traps. *Chem. Eng. J.* **2009**, *154*, 211–218. [[CrossRef](#)]
41. Wang, F.; Zhang, T.T.; You, R.; Chen, Q. Evaluation of Infection Probability of Covid-19 in Different Types of Airliner Cabins. *Build. Environ.* **2023**, *234*, 110159. [[CrossRef](#)]
42. Park, S.; Mistrick, R.; Rim, D. Performance of Upper-Room Ultraviolet Germicidal Irradiation (UVGI) System in Learning Environments: Effects of Ventilation Rate, UV Fluence Rate, and UV Radiating Volume. *Sustain. Cities Soc.* **2022**, *85*, 104048. [[CrossRef](#)]
43. Shao, X.; Wen, X.; Paek, R.; Liu, Y.; Jian, Y.; Liu, W. Use of Recirculated Air Curtains inside Ventilated Rooms for the Isolation of Transient Contaminant. *Energy Build.* **2022**, *273*, 112407. [[CrossRef](#)]
44. Ren, C.; Xi, C.; Wang, J.; Feng, Z.; Nasiri, F.; Cao, S.J.; Haghghat, F. Mitigating COVID-19 Infection Disease Transmission in Indoor Environment Using Physical Barriers. *Sustain. Cities Soc.* **2021**, *74*, 103175. [[CrossRef](#)]
45. Ren, C.; Zhu, H.C.; Cao, S.J. Ventilation Strategies for Mitigation of Infection Disease Transmission in an Indoor Environment: A Case Study in Office. *Buildings* **2022**, *12*, 180. [[CrossRef](#)]
46. D'Alicandro, A.C.; Mauro, A. Effects of Operating Room Layout and Ventilation System on Ultrafine Particle Transport and Deposition. *Atmos. Environ.* **2022**, *270*, 118901. [[CrossRef](#)]
47. Yan, Y.; Li, X.; Ito, K. Numerical Investigation of Indoor Particulate Contaminant Transport Using the Eulerian-Eulerian and Eulerian-Lagrangian Two-Phase Flow Models. *Exp. Comput. Multiph. Flow* **2020**, *2*, 31–40. [[CrossRef](#)]
48. Pei, G.; Taylor, M.; Rim, D. Human Exposure to Respiratory Aerosols in a Ventilated Room: Effects of Ventilation Condition, Emission Mode, and Social Distancing. *Sustain. Cities Soc.* **2021**, *73*, 103090. [[CrossRef](#)]
49. Zhao, B.; Yang, C.; Yang, X.; Liu, S. Particle Dispersion and Deposition in Ventilated Rooms: Testing and Evaluation of Different Eulerian and Lagrangian Models. *Build. Environ.* **2008**, *43*, 388–397. [[CrossRef](#)]
50. Chen, F.; Yu, S.C.; Lai, A.C. Modeling Particle Distribution and Deposition in Indoor Environments with a New Drift-Flux Model. *Atmos. Environ.* **2006**, *40*, 357–367. [[CrossRef](#)]
51. D'Alicandro, A.C.; Mauro, A. Air Change per Hour and Inlet Area: Effects on Ultrafine Particle Concentration and Thermal Comfort in an Operating Room. *J. Aerosol Sci.* **2023**, *171*, 106183. [[CrossRef](#)]
52. Feng, Y.; Li, D.; Marchisio, D.; Vanni, M.; Buffo, A. A Computational Fluid Dynamics—Population Balance Equation Approach for Evaporating Cough Droplets Transport. *Int. J. Multiph. Flow* **2023**, *165*, 104500. [[CrossRef](#)]
53. Crowe, C.T.; Schwarzkopf, J.D.; Sommerfeld, M.; Tsuji, Y. *Multiphase Flows with Droplets and Particles*, 2nd ed.; CRC Press: Boca Raton, FL, USA, 2012. [[CrossRef](#)]
54. Marchisio, D.L.; Fox, R.O. *Computational Models for Polydisperse Particulate and Multiphase Systems*; Cambridge Series in Chemical Engineering; Cambridge University Press: Cambridge, MA, USA, 2013. [[CrossRef](#)]
55. Balachandar, S.; Eaton, J.K. Turbulent Dispersed Multiphase Flow. *Annu. Rev. Fluid Mech.* **2010**, *42*, 111–133. [[CrossRef](#)]
56. Subramaniam, S. Lagrangian–Eulerian Methods for Multiphase Flows. *Prog. Energy Combust. Sci.* **2013**, *39*, 215–245. [[CrossRef](#)]
57. Capecelatro, J.; Desjardins, O. An Euler–Lagrange Strategy for Simulating Particle-Laden Flows. *J. Comput. Phys.* **2013**, *238*, 1–31. [[CrossRef](#)]
58. Biswas, R.; Pal, A.; Pal, R.; Sarkar, S.; Mukhopadhyay, A. Risk Assessment of COVID Infection by Respiratory Droplets from Cough for Various Ventilation Scenarios inside an Elevator: An OpenFOAM-Based Computational Fluid Dynamics Analysis. *Phys. Fluids* **2022**, *34*, 013318. [[CrossRef](#)] [[PubMed](#)]
59. ESI-OpenCFD. ESI OpenCFD Release OpenFOAM® V2106. 2021. Available online: <https://www.openfoam.com/news/main-news/openfoam-v2106> (accessed on 9 July 2025).
60. Zhang, T.T.; Lee, K.; Chen, Q.Y. A Simplified Approach to Describe Complex Diffusers in Displacement Ventilation for CFD Simulations. *Indoor Air* **2009**, *19*, 255–267. [[CrossRef](#)]
61. King, M.F.; Noakes, C.J.; Sleigh, P.A. Modeling Environmental Contamination in Hospital Single- and Four-Bed Rooms. *Indoor Air* **2015**, *25*, 694–707. [[CrossRef](#)]

62. Yakhot, V.; Orszag, S.A.; Thangam, S.; Gatski, T.B.; Speziale, C.G. Development of Turbulence Models for Shear Flows by a Double Expansion Technique. *Phys. Fluids A Fluid Dyn.* **1992**, *4*, 1510–1520. [[CrossRef](#)]
63. Yuce, B.E.; Pulat, E. Forced, Natural and Mixed Convection Benchmark Studies for Indoor Thermal Environments. *Int. Commun. Heat Mass Transf.* **2018**, *92*, 1–14. [[CrossRef](#)]
64. D’Alicandro, A.C.; Mauro, A. Experimental and Numerical Analysis of CO<sub>2</sub> Transport inside a University Classroom: Effects of Turbulent Models. *J. Build. Perform. Simul.* **2023**, *16*, 434–459. [[CrossRef](#)]
65. Cheng, Y.; Lin, Z. Experimental Study of Airflow Characteristics of Stratum Ventilation in a Multi-Occupant Room with Comparison to Mixing Ventilation and Displacement Ventilation. *Indoor Air* **2015**, *25*, 662–671. [[CrossRef](#)] [[PubMed](#)]
66. Zhang, Z.; Chen, Q. Experimental Measurements and Numerical Simulations of Particle Transport and Distribution in Ventilated Rooms. *Atmos. Environ.* **2006**, *40*, 3396–3408. [[CrossRef](#)]

**Disclaimer/Publisher’s Note:** The statements, opinions and data contained in all publications are solely those of the individual author(s) and contributor(s) and not of MDPI and/or the editor(s). MDPI and/or the editor(s) disclaim responsibility for any injury to people or property resulting from any ideas, methods, instructions or products referred to in the content.